

## Understanding the effect of structural changes on slow magnetic relaxation in mononuclear octahedral copper(II) complexes

Dawid Marcinkowski<sup>a#</sup>, Ariel Adamski<sup>a#</sup>, Maciej Kubicki<sup>a</sup>, Giuseppe Consiglio<sup>b</sup>, Violetta Patroniak<sup>a</sup>, Tomasz Ślusarski<sup>a,c</sup>, Muhammed Açıkgöz<sup>d</sup>, Daria Szeliga<sup>e</sup>, Nahir Vadra<sup>a,f</sup>, Mirosław Karbowski<sup>e</sup>, Ireneusz Stefaniuk<sup>g</sup>, Czesław Rudowicz<sup>a</sup>, Adam Gorczyński<sup>a\*</sup> and Maria Korabik<sup>e\*</sup>

<sup>a</sup>Faculty of Chemistry, Adam Mickiewicz University, Uniwersytetu Poznańskiego 8, 61-614 Poznań, Poland

<sup>b</sup>Dipartimento di Scienze Chimiche, Università di Catania, I-95125 Catania, Italy

<sup>c</sup>Institute of Spintronics and Quantum Information, Faculty of Physics, Adam Mickiewicz University, Uniwersytetu Poznańskiego 2, 61-614 Poznań, Poland

<sup>d</sup>Department of Science, The State University of New York (SUNY) Maritime College, New York 10465, USA.

<sup>e</sup> Faculty of Chemistry, University of Wrocław, F. Joliot-Curie 14, 50-383 Wrocław, Poland

<sup>f</sup> Universidad de Buenos Aires, Facultad de Ciencias Exactas y Naturales, Departamento de Química Inorgánica, Analítica y Química Física and CONICET–Universidad de Buenos Aires, Instituto de Química Física de los Materiales, Medio Ambiente y Energía (INQUIMAE), Buenos Aires C1428EGA, Argentina

<sup>g</sup> College of Natural Sciences, University of Rzeszow, Rejtana 16a, 35-310 Rzeszow, Poland

## Supplementary Information

### Table of contents:

<b>I.</b>	<b>General information</b>	<b>S4</b>
<b>II.</b>	<b>Experimental section – synthesis, X-ray data, magnetic studies</b>	<b>S8</b>
<b>Figure S1</b>	<b>Experimental and simulated PXRD spectra of compounds 1 and 2</b>	<b>S9</b>
<b>Table S1</b>	<b>Crystal data, data collection and structure refinement</b>	<b>S9</b>
<b>Table S2</b>	<b>Relevant geometrical parameters (Å, °) with s.u.'s in parentheses</b>	<b>S10</b>
<b>Table S3</b>	<b>Hydrogen bond data (Å, °)</b>	<b>S10</b>
<b>Table S4</b>	<b>SHAPE analysis for 6-coordinated copper(II) complexes that exhibit slow relaxation of magnetization</b>	<b>S11</b>
<b>Table S5</b>	<b>SHAPE analysis for 1 and 2 assuming coordination number 4 as a function of different square planar planes.</b>	<b>S11</b>
<b>Figure S2</b>	<b>Temperature dependence of magnetic susceptibility and <math>\chi_m T</math> product of 1(left) and 2 (right)</b>	<b>S12</b>
<b>Figure S3</b>	<b>Magnetization versus magnetic field, measured at 2 K of both compounds, 1 (left), 2 (right). Solid red lines show theoretical Brillouin function for <math>S = \frac{1}{2}</math> and <math>g = 2</math></b>	<b>S12</b>
<b>Figure S4</b>	<b>Out of phase susceptibility <math>\chi''</math> versus magnetic field relation for complex 1</b>	<b>S12</b>
<b>Figure S5</b>	<b>Out of phase susceptibility <math>\chi''</math> versus magnetic field frequency relation for complex 1 (left) and 2 (right)</b>	<b>S13</b>
<b>Figure S6</b>	<b>Analysis of the relaxation time of 1.</b>	<b>S13</b>
<b>Table S6</b>	<b>Parameters from Debye model of complex 1</b>	<b>S13</b>
<b>III.</b>	<b>CW-EPR</b>	<b>S14</b>
<b>Figure S7</b>	<b>The temperature dependence of Q-band EPR spectra for complex 1</b>	<b>S14</b>
<b>Figure S8</b>	<b>The temperature dependence of Q-band EPR spectra for complex 2</b>	<b>S15</b>

Figure S9	X-band (300K and 90K) and Q-band (10K) EPR spectra of 1 (a) and 2 (b) at 300K, 90K and 10K temperatures. Solid blue line shows simulated spectrum; for complex 2 simulations were based on the use of one component only.	S16
Figure S10	X-band EPR spectra for the Cu(II) ion in complexes 1 (red) and 2 (blue) at 300 K	S17
Figure S11	The line width $B_{pp}$ the EPR lines for complexes 1 (red) and 2 (blue)	S18
Figure S12	Temperature dependence of the inverse total EPR line intensity on the for complexes 1 and 2	S18
Figure S13	Experimental (exp) and fitted (fit) EPR spectrum using one spectral component only for complex 2 at 300 K	S19
Figure S14	Experimental (exp) and fitted (fit) EPR spectrum using one spectral component only for complex 2 at 91 K	S20
Figure S15	Experimental (exp) EPR spectrum for complex 2 and spectra simulated using: (i) simulations of separate lines (A, B) and (ii) combined simulations of both spectral components (comb) at 300 K	S20
Figure S16	Experimental (exp) EPR spectrum for complex 2 and spectra simulated using: (i) simulations of separate lines (A,B) and (ii) combined simulations of both spectral components (comb) at 91 K	S21
Figure S17	Energy levels for complex 1 at resonance frequency 9.42108 GHz with $B_0  z$ . Red lines show all possible transitions with probability equal 1 generated automatically by EasySpin program	S22
Figure S18	Energy levels for complex 1 at resonance frequency 9.42108 GHz with $B_0$ in the xy-plane. Red lines show all possible transitions with probability from 0.98 to 1.0, blue lines - with probability from 0.0015 to 0.0026 generated automatically by EasySpin program	S22
Table S7	Energy levels (ELs, in GHz) associated with the transitions at the resonance field ( $B_{res}$ ) indicated in Figures S17 and S18 for complexes 1 and 2	S22
Table S8	Energy levels (ELs, in GHz) associated with the transitions at the resonance field ( $B_{res}$ ) indicated in Figures S17 and S18 for complex 2 and two components A and B	S23
Figure S19	Hyperfine energy levels of Cu(II) ions in a coordination compound with allowed transitions indicated	S23
Scheme S1	Graphical representation of the origin of the presumed Cu(I)NO nitrosyl-related radicals. Coordinated solvent molecule and counterions are omitted for clarity.	S24
Figure S20	Temperature dependence of the $g_{eff}$ factor for the complexes 1 and 2	S24
Figure S21	Temperature dependence of the line width $B_{pp}$ for the complexes 1 and 2	S25
Figure S22	X-ray graphical representations of crystallographically equivalent but magnetically inequivalent Cu(II) pairs of 1 and 2	S25
Figure S23	The averaged EPR powder spectrum obtained from PHI simulations using integration over several directions of magnetic field, for linewidth equal to 0.1 GHz, 0.15 GHz, 0.6 GHz along the x-, y-, z-axis, respectively. The indicated transition corresponds to the magnetic field directed along the x direction	S27
Figure S24	EPR spectrum obtained from PHI simulations using integration over three main directions of magnetic field, for linewidth equal to 0.05 GHz, 0.15 GHz, 0.6 GHz along the x-, y-, z-axis, respectively. The indicated transitions correspond from upper to lower to the magnetic field directed along the x-, y-, and z direction, respectively	S28
IV.	Optical spectroscopy	S29
Figure S25	Absorption spectrum for the thin film of 1 measured at RT	S30
Figure S26	Coordination of the nearest ligands around Cu(II) ion in: (a) the complex 1 and (b) 2. The adopted Cartesian molecular axis system (CMAS) (X, Y, Z) reveals the approximate $C_2$ symmetry of Cu(II) center	S30

Figure S27	Deconvolution of the spectrum of 1 into 3 bands	S31
Figure S28	Absorption spectrum for the thin film of 1 and 2 measured at RT	S31
V.	Definitions of the axis systems (ASs) and input sets used for computational modelling of complex 1 and 2	S32
Table S9	The atomic positions ( $\phi$ , $\theta$ , $R$ ) within the $ML_n$ complex expressed in the CMAS ( $X$ , $Y$ , $Z$ ) defined in Figure S26 for sets $C_1$ and $C_{2v}$	S32
VI.	Computations using ab initio methods	S34
Figure S29	$\chi T$ plots versus temperature calculated with NEVPT2 for both compounds	S35
Table S10	Results of Mulliken populations for selected atoms (denoted by cif symbols) calculated using B3LYP DFT and CASSCF for complexes 1 and 2. Charges are in units of $ e $ and spin in Bohr magnetons.	S35
Table S11	Mulliken populations for selected atoms calculated using B3LYP for complex 1 and basis set ZORA-def2-SVP with exception of (*), where basis is def2-SPV. Charges are in units of $ e $ and spin in Bohr magnetons; notation of atoms (symbol and number) is as in cif file	S36
Table S12	Mulliken populations for selected atoms calculated using CAM-B3LYP for complex 1; charge is in units of $ e $ and spin is in Bohr magnetons	S36
Table S13	Energies of the excited states w.r.t. the ground state (in $cm^{-1}$ ) calculated using CAM-B3LYP for complex 1; results for B3LYP are shown for comparison	S36
Table S14	Mulliken, Loewdin and Mayer populations for selected atoms of complexes 1 and 2 calculated using CASSCF approach. Basis sets is of ZORA-def2-SVP with exception of *where basis is def2-SPV. Charges are in units of $ e $ and spin in Bohr magnetons; notation of atoms (symbol and number) is as in cif file	S36
Table S15	Energies of Kramers doublet (KD) states (in $cm^{-1}$ ) for complexes 1 and 2.	S37
Table S16	Composition of spin-orbit relativistic states being linear combinations of the nonrelativistic NEVPT2 states mixed by SOC, which are denoted as: $ number\ of\ root, S, M_S\rangle$ . Only states with major weights are listed. Number of root means the consecutive number of NEVPT2 state (0 is ground state (GS), 1 is 1 <sup>st</sup> excited state etc.)	S37
Table S17	The $A$ -tensor components (in $10^{-4} cm^{-1}$ ) for complex 1 obtained using ZORA approach and DKH one (including SOC correction of the 0 <sup>th</sup> or 2 <sup>nd</sup> order)	S37
Table S18	Orbital energies (in $cm^{-1}$ ) calculated using ab initio Ligand Field for complexes 1 and 2. Orbitals expressed as the real 3d functions correspond to respective LF states.	S38
VII.	SPM and MSH analysis	S39
Table S19	The conventional CFPs calculated using the CFPs $B_{kq}$ in Table 5 together with energy levels: $E_i$ (all in $cm^{-1}$ ) and SHPs: $g_i$ (dimensionless) and $A_i$ (in $10^{-4} cm^{-1}$ ).	S40
Table S20	The axial $g_i$ (dimensionless) and hyperfine parameters $A_i$ (in $10^{-4} cm^{-1}$ ) reported for Cu(II) ions in various compounds.	S41
VIII.	Literature	S42

## I. General Information

All chemicals (the metal salts, organic compounds, solvents) were purchased from Merck Chemical Company or POCH as analytical grade and used without further purification. Precoated aluminum sheets (Silica gel 60 F254, Merck) were used for thin-layer chromatography (TLC), while the spots were visualized under UV light (BVL-6LC, Vilber) with a wavelength of 254 nm. Column Chromatography (CC) was performed for the purification of the organic products, using 70–230 mesh silica gel particles. Elemental analyses were performed on Elementar Analyser Vario EL III (CHNS) and the results are within  $\pm 0.3\%$  of the theoretical values. Fourier Transform Infrared (FT-IR) spectra were performed by means of a FT-IR Bruker IFS 66v/S spectrophotometer, in the range between 400 and 4000  $\text{cm}^{-1}$  with a resolution of 4  $\text{cm}^{-1}$ . An average of 24 scans has been carried out for each sample. The samples were prepared on a KBr pellet under a pressure of 0.01 torr. Mass spectra (ESI-MS) were determined by a Waters Micromass ZQ spectrometer in acetonitrile or methanolic solutions with concentrations  $\sim 10^{-4}$  M. The samples were run in the positive-ion mode. Sample solutions were introduced into the mass spectrometer source with a syringe pump with a flow rate of 40  $\mu\text{L min}^{-1}$  with a capillary voltage of +3 kV and a desolvation temperature of 300°C. Source temperature was 120°C. Cone voltage ( $V_c$ ) was set to 30 V to allow transmission of ions without fragmentation processes. Scanning was performed from  $m/z = 100$  to 1000 for 6 s, and 10 scans were summed to obtain the final spectrum. The synthesis of 2,6-pyridinedicarboxaldehyde (A) was performed following a previously published procedure.<sup>1</sup>

**X-ray crystallography** Diffraction data were collected by the  $\omega$ -scan technique at room temperature (**1**) or at 100(1) K (**1'**, **2**) on Rigaku XCalibur four-circle diffractometer with Eos CCD detector and graphite-monochromatized  $\text{MoK}_\alpha$  radiation ( $\lambda=0.71073$  Å). The data were corrected for Lorentz-polarization as well as for absorption effects.<sup>2</sup> Precise unit-cell parameters were determined by a least-squares fit of 10512 (**1**), 7586 (**1'**) and 5533 (**2**) reflections of the highest intensity, chosen from the whole experiment. The structures were solved with SHELXT-2013<sup>3</sup> and refined with the full-matrix least-squares procedure on  $F^2$  by SHELXL-2013.<sup>3</sup> All non-hydrogen atoms were refined anisotropically, hydrogen atoms were placed in idealized positions and refined as 'riding model' with isotropic displacement parameters set at 1.2 (1.5 for methyl groups) times  $U_{\text{eq}}$  of appropriate carrier atoms. The crystals of **1** displayed very weak diffraction only (despite the number of tries) and therefore the quality of this structure determination is relatively low, but anyway good enough for determination of general structural features; the low temperature structure of **1'** also confirms reliability of measurement of structure **1**; in the structure of **2** the solvent methanol molecules were found disordered over two positions with site occupation factors of 69.3(7)/30.7(7)%. The shapes of displacement ellipsoids within the disordered fragment were subjected to rigid-bond restraints (RIGU). Relevant experimental data and refinement details are reported in Table S1. Crystallographic data for the structural analysis has been deposited with the Cambridge Crystallographic Data Centre, Nos. CCDC-1965451, CCDC-1965452 and CCDC-2150965. Copies of this information may be obtained free of charge from: The Director, CCDC, 12 Union Road, Cambridge, CB2 1EZ, UK. Fax: +44(1223)336-033, e-mail: deposit@ccdc.cam.ac.uk, or [www.ccdc.cam.ac.uk](http://www.ccdc.cam.ac.uk).

**Powder X-Ray diffraction (PXRD).** PXRD analyses were performed using a Bruker AXS D8 Advance diffractometer. A powdered microcrystalline sample was ground in an agate mortar and was deposited in the hollow of a quartz zero-background plate.

**Nuclear Magnetic Resonance.** Nuclear magnetic resonance ( $^1\text{H}$  and  $^{13}\text{C}$  NMR) were recorded on a Mercury-plus-400 MHz spectrometer and calibrated against the residual protonated solvent signals ( $\text{CDCl}_3$ :  $\delta=7.26$  and  $\text{CD}_3\text{CN-}d_3$ :  $\delta=1.94$ ), given in *ppm*.

**Electron Magnetic Resonance.** In order to immobilize our samples microcrystalline powder was placed in a 1mm thin-walled quartz capillary and "pressed / squeezed", then positioned with quartz wool on both sides. This prevents reorientation with respect to the magnetic field due to the "loosening" of powder and thus ensures keeping the sample in the right position. The parameters pertaining to registering of EMR spectra are: X- band (Frequency 9.42 GHz, Power 94.64 mW); Q-band (Frequency 33.92 GHz, Power 12.62 mW). Initial X-band EPR spectra of powdered microcrystalline sample were measured at 295 K and at 77 K using a Bruker Elexys E 500 Spectrometer equipped with an NMR tesla meter and a frequency counter. The experimental spectra were simulated using the computer program DoubletExact ( $S = \frac{1}{2}$ ) (using calculation of resonance fields by diagonalization of the energy matrix) written by Prof. Andrew Ozarowski from National High Magnetic Field Laboratory, Florida State University, Tallahassee, USA. Subsequent X (300 K – 90 K) and Q (300 K – 4 K) band studies were measured using Bruker ELEXSYS E580 equipped with Hall probe for induction control for CW mode and simulated using EasySpin program.<sup>4,5</sup> All fittings were performed several times for each case, starting from different input data, and

as a result, similar final values were obtained with an accuracy of 3%. Hence, the final results were selected taking into account the best fits, i.e. those with the lowest RMSD value.

**SQUID Magnetometry.** Magnetization measurements in the temperature range of 1.8–300 K at the magnetic field of 0.5 T and field dependent magnetization measurements in an applied magnetic field from 0 to 5 T at 2 K were carried out for a sample of powdered crystals of compounds (0.04468 g **1** and 0.0480 g **2**, using a Quantum Design SQUID Magnetometer (type MPMS-3). The AC measurements of **1** and **2** were made under 0.1 T DC field and at  $3 \cdot 10^{-4}$  T oscillating field, in the temperature and frequency range:  $T = 1.8 - 10$  K,  $\nu = 1 - 996$ , Hz respectively. The magnetic data were corrected for the sample holder (Quantum Design Clear Plastic Straws in Paper-AGC2, free of paramagnetic impurities). Corrections for diamagnetism of the constituting atoms were calculated using Pascal's constants<sup>6</sup>, the value of  $60 \cdot 10^{-6}$  cm<sup>3</sup>mol<sup>-1</sup> was used as the temperature-independent paramagnetism of Cu(II) coordination polymers.<sup>7</sup>

**Optical Spectroscopy.** The absorption spectra were recorded in the 800 - 200 nm range at 4.2 K on a Cary-5000 UV-Vis-NIR spectrophotometer, equipped with an Oxford Instrument model CF1204 cryostat. In order to obtain the spectrum a well ground mixture of samples with some silicon grease were placed between two quartz plates, approximately 1 cm in diameter, and pressed to get a transparent layer.

### Computational Studies.

**Ab initio approaches.** We have calculated electronic structure of complexes **1** and **2** using ORCA 4.2.1 code<sup>8,9</sup> for the experimental X-ray structural data. For the sake of comparison to semiempirical results we have rotated and translated coordinates from .cif file to put Cu atom in the center of computational cell and set Cartesian axes almost along the bonds between Cu and its nearest neighbors (see Section 2.8). We have used basis ZORA-def2-SVP, suited to relativistic calculations. Firstly, we have used B3LYP<sup>10</sup> exchange-correlation potential to calculate DFT magnetic ground state. Then the resulting unrestricted orbitals were used as a starting point to CASSCF<sup>11</sup> calculations with allowed 9 electrons to occupy 5 orbitals since we assume the nominal oxidicity of copper atom as 2+. Active space consisting of 5 orbitals was chosen as the set of orbitals with major contribution from 3d orbitals of copper atom. We were considering 5 Kramers doublets in such calculations with no frozen orbitals. Consequently, NEVPT2<sup>12</sup> calculations were done for all states, to account for dynamical correlations. Furthermore we have calculated excited states using time-dependent DFT (TDDFT) methods<sup>13-15</sup>, where we have used long-range potential CAM-B3LYP<sup>16</sup>. We have also accounted for scalar relativistic corrections and included spin-orbit coupling (SOC) operator that mixes states<sup>17</sup>. For that purpose we use two methods: (i) 0th-order regular approximation (ZORA)<sup>18</sup> and (ii) Douglas-Kroll-Hess (DKH)<sup>19</sup>. The SOC could be included within ZORA approach or as 1<sup>st</sup> or 2<sup>nd</sup> order DKH transformation of SOC operator<sup>20,21</sup>.

Within procedures implemented in Orca<sup>9,22</sup> we compute parameters of effective models based on ab initio results for comparison with phenomenological models. Since we model molecule as one-center magnetic  $S = \frac{1}{2}$  system, the only magnetic anisotropic behavior seen in experimental data could be interpreted as the anisotropy of  $g$ -tensor or  $A$ -tensor. The tensors  $g$  and  $A$  are computed using effective models relying on the SOC operators which are computed at default from densities calculated from scalar (quasi)relativistic equations. Effective SOC operators are computed with inclusion of so called picture-change effect, which transforms relativistic operator to be fully consistent with used (quasi)relativistic equations. This has been done with either 0th-order regular approximation (ZORA) or (up to 2<sup>nd</sup> order) DKH Douglas-Kroll-Hess transformation of SOC operator. We have also derived parameters of Ligand Field model to describe optical spectrum<sup>23,24</sup>

**SPM and MSH analysis.** To complement ab initio modelling (see Section 2.9) semiempirical modelling is carried out for Cu(II) centers in **1** and **2** utilizing two approaches: (1) superposition model (SPM)<sup>25,26</sup> analysis of the CFPs (SPM/CFP) in Wybourne notation ( $B_{kq}$ )<sup>25,27,28</sup> and (2) microscopic spin Hamiltonian (MSH) calculations of the SH parameters (SHPs)<sup>29-33</sup>. Notations for the Hamiltonians  $H_{SH}$  and  $H_{CF}$  and the associated parameters were defined below. The SPM/CFP predictions (approach 1) are carried out using the set denoted  $C_{2v}$  in Section III in SI. These results provide input into the relations for the energy differences between the excited states and the ground state expressed in terms of CFPs<sup>34-40</sup>. Subsequently, the MSH formulas (approach 2) for Cu(II;  $3d^9$ ) derived from the higher order perturbation theory<sup>34-40</sup> were utilized to calculate SHPs, i.e. the spectroscopic splitting factors  $g_i$  and the hyperfine splitting parameters  $A_i$ . These MSH utilize knowledge of the energy levels, the spin-orbit coupling constant  $\zeta$ , and other microscopic parameters. To consider the ascent/descent in symmetry method<sup>41-43</sup>, the approximated MSH formulas<sup>34-40</sup> suitable for tetragonal and orthorhombic symmetry are employed. Further computational details and results are provided in the Section 2.10 in manuscript.

**Notations used for spin Hamiltonian (SH) and crystal field (CF) Hamiltonian.** Two major branches of spectroscopy being of interest to this study are optical spectroscopy<sup>44-46</sup>, and electron magnetic resonance (EMR) spectroscopy<sup>29-31</sup>. Hence, two major types of Hamiltonians are considered herein: (i) the crystal field (CF) (or ligand field, LF) Hamiltonians  $H_{CF}$  together with the free-ion Hamiltonians  $H_{FI}$ , which are used to describe optical spectra of transition ions in crystals<sup>44-46</sup>, and (ii) the spin Hamiltonians (SH), which include the Zeeman electronic (Ze) term  $H_{Ze}$ , hyperfine interaction (HFI) between electronic spin  $S$  and nuclear spin  $I$  ( $H_{HFI}$ ), and the zero-field splitting (ZFS) Hamiltonians ( $H_{ZFS}$ ), which are used to describe EMR spectra<sup>29-31</sup>. Note that for Cu(II) ion:  $S = 1/2$ ,  $I = 3/2$ , hence no ZFS terms apply, whereas only one ground multiplet  $^2D$  exists. To describe EMR spectra of ions in crystals and transitions between spin states<sup>29-31</sup> the concept of an effective spin Hamiltonian (SH) has been introduced:<sup>33, 47</sup>

$$H_{SH} = H_{Ze} + H_{HFI} = \mu_B B \cdot g \cdot \tilde{S} + \mu_B I \cdot A \cdot \tilde{S} \quad (1)$$

where  $g$  is the Zeeman factor and  $A$  is the hyperfine tensor. For orthorhombic symmetry as well as in the principal axis system for monoclinic or triclinic symmetry only the components (x, y, z) exist in Eq. (1), whereas for axial symmetry:  $g_{\parallel}$ ,  $g_{\perp}$  and  $A_{\parallel}$ ,  $A_{\perp}$ . In terms of the Wybourne (Wyb) operators<sup>48, 49</sup>, i.e. the normalized spherical operators  $C_q^{(k)}$  ( $C_{kq}$ ),  $H_{CF}(H_{LF})$  within the whole  $d^N$  or  $f^N$  configuration may be represented in two general forms, i.e. compact and expanded. In the **compact** form<sup>33</sup>, i.e. with  $-k \leq q \leq +k$ , the **triclinic**  $H_{CF}(H_{LF})$  may be given in several equivalent representation, most commonly as:<sup>33, 41, 48, 49</sup>

$$H_{CF}(Wyb) = \sum_{kq} B_{kq} C_q^{(k)} \equiv \sum_{kq} B_{kq} C_{kq} \equiv \sum_{kq} B_q^k C_q^{(k)} \quad (2)$$

where the CF parameters (CFPs)  $B_{kq}$  ( $B_q^k$ ) are in general complex, except for  $q = 0$ , and  $C_q^{(k)}$  ( $C_{kq}$ 's) are to be summed over all unpaired electrons of the unfilled shell of the RE (TM) ion, i.e.:  $C_q^{(k)} = \sum_i C_q^k(\theta_i, \varphi_i)$ . The conversion relations between  $B_k^q(ESO)$  in Eq. (5) and  $B_{kq}(Wyb)$  in Eq. (2) may be found in, e.g.<sup>33, 48, 49</sup>. In the **expanded** form<sup>33, 48, 49</sup>, i.e. with  $0 \leq q \leq +k$ , the **triclinic**  $H_{CF}$  is equivalently given as:

$$H_{CF}(Wyb) = \sum_k \left[ B_{k0} C_0^{(k)} + \sum_{q=1}^k \left( \text{Re } B_{kq} \left( C_{-q}^{(k)} + (-1)^q C_q^{(k)} \right) + i \text{Im } B_{kq} \left( C_{-q}^{(k)} - (-1)^q C_q^{(k)} \right) \right) \right] \quad (3)$$

The real parts  $ReB_{kq}$  and the imaginary  $ImB_{kq}$  parts of the complex CFPs  $B_{kq}$  in Eq. (2) are often replaced in Eq. (3) by the symbols  $B_{kq}$  and  $B_{k-q}$ , respectively, yielding a simplified form (with  $0 \leq q \leq +k$ ):

$$H_{CF}(Wyb) = \sum_k \left[ B_{k0} C_0^{(k)} + \sum_{q=1}^k \left( B_{kq} \left( C_{-q}^{(k)} + (-1)^q C_q^{(k)} \right) + i B_{k-q} \left( C_{-q}^{(k)} - (-1)^q C_q^{(k)} \right) \right) \right] \quad (4)$$

The notation in Eq. (4) is adopted in semiempirical modelling in Section 2.10. Caution is needed to avoid unintended ambiguities with the symbols in Eq. (2) when comparing CFP sets reported in literature. The simplified crystal field (CF) Hamiltonian for  $3d^N$  ions, acting only within the ground multiplet  $^{2S+1}L$ , has the form:<sup>33</sup>

$$H_{CF}(ESO) = \sum_{k,q} B_k^q O_k^q(\mathbf{J} \text{ or } \mathbf{L}) = \sum_{k,q} A_k^q \langle r^k \rangle \theta_k O_k^q = \sum_{k,q} C_k^q \theta_k O_k^q \quad (5)$$

where  $O_k^q$  denote the extended Stevens operators (ESO)<sup>50, 51</sup> and  $B_k^q$  ( $A_k^q$ ,  $C_k^q$ ) - the CF parameters (CFPs), which are all real, whereas the so-called multiplicative Stevens factors  $\theta_k = \alpha$ ,  $\beta$ , and  $\gamma$  for the rank  $k = 2$ , 4, and 6, respectively, are tabulated, see, e.g. (4). The first form in Eq. (5) is utilized in MOLCAS<sup>52</sup> and PHI<sup>53</sup> for  $H_{CF}(H_{LF})$  (and with the spin operator ( $S$ ) for  $H_{ZFS}$ ). Hence the notation in Eq. (5) will be used for presentation of CFPs modelled using ab initio methods. The summation in Eq. (2) and (5) includes all  $q$  components:  $-k \leq q \leq +k$ , whereas specific limits on the non-zero components  $q$  are governed by the local site symmetry and group theory.<sup>33</sup> The limit to the ranks  $k$  ( $k \leq 2l$ ) for the operators acting within

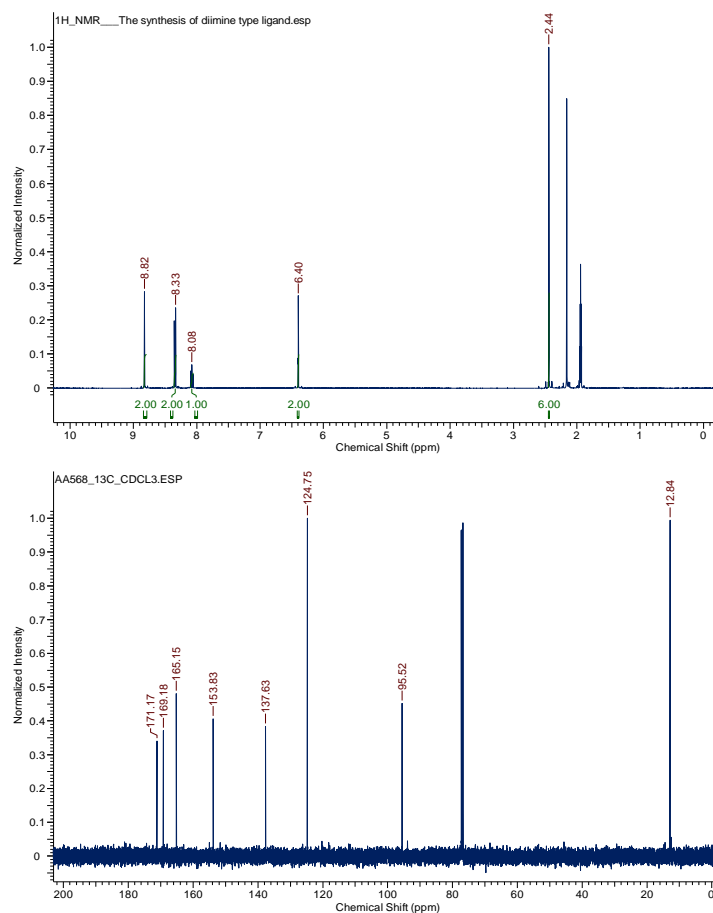
the ground multiplet and the associated CFPs arises from the orbital quantum number ( $l$ ) of a given configuration, namely,  $J(f^N)$ :  $l = 3$  yields  $k = 2, 4,$  and  $6$  or  $L(d^N)$ :  $l = 2$  yields  $k = 2$  and  $4$ .

## II. Experimental section – synthesis, X-ray data, magnetic studies

### The imination of 2,6-pyridinedicarboxaldehyde with 3-amino-5-methylisoxazole (**L**)

2,6-pyridinedicarboxaldehyde (**A**) (1.000 g, 7.4 mM) and 3-amino-5-methylisoxazole (**B**) (1.488 g, 15.2 mM) were weighed into a round-bottomed flask, which was fitted with a Dean-Stark cap. After flushing with argon, the anhydrous toluene (60 mL) was added and the resulting mixture was stirred at 140°C for 6 hours. The solution in the flask was concentrated (by Dean Stark's tap) and allowed to slowly cool to the room temperature for the crystallization of the product. The crystallite was filtered and washed with cold toluene. Drying in the air gave white crystals of the ligand **L** with yield of 44% (0.930g, 3.1mM).

$^1\text{H}$  NMR (400 MHz,  $\text{CD}_3\text{CN}$ ):  $\delta$  8.82 (2H, d,  $J = 0.58$ ),  $\delta$  8.35-8.33 (2H, d,  $J = 7.77$ ), 8.08 (1H, tt,  $J = 7.52, 0.66, 0.58$ ); 6.40 (2H, q,  $J = 7.52, 0.83, 0.91$ ); 2.44 (1H, d,  $J = 0.91$ );  $^{13}\text{C}$  NMR (400 MHz,  $\text{CDCl}_3$ ):  $\delta$  171.2, 196.2, 165.2, 153.8, 137.6, 124.8, 95.5, 12.8; FT-IR (KBr,  $\text{cm}^{-1}$ ):  $\nu(\text{O-H})$  3477;  $\nu(\text{N-H})$  3385, 3195;  $\nu(\text{C-H})_{\text{arom}}$  3066, 3003;  $\nu_{\text{as}}(\text{C-H})_{\text{alif}}$  2927;  $\nu_{\text{s}}(\text{C-H})_{\text{alif}}$  2891;  $\nu(\text{C}=\text{C})$  1716, 1629, 1606, 1580, 1566, 1551, 1470;  $\nu(\text{C}=\text{N})$  1450, 1429, 1396;  $\delta(\text{CH}_3)$  1328;  $\nu(\text{C-O})$  1253, 1223;  $\gamma(\text{C-H})_{\text{arom}}$  1158, 1134, 1077, 1048, 1009, 992, 965, 932, 924, 850, 823, 807, 785, 740, 697, 671, 646, 626, 596. ESI-MS(+)  $m/z$  (%): 296 (100)  $[\text{LH}]^+$ , 382 (12)  $[\text{L}(\text{CH}_3\text{OH})_2\text{Na}]^+$ ; Anal. calc. for  $[\text{C}_{15}\text{H}_{13}\text{N}_5\text{O}_2]$  (295.30); C, 61.01; H, 4.44; N, 23.72; O, 10.84, found: % C, 61.36; H, 4.26; N, 24.21 %.



$^1\text{H}$  NMR and  $^{13}\text{C}$  NMR spectra of **L**.

### Synthesis of complex 1

The solution of copper(II) perchlorate hexahydrate (0.113 g, 0.30 mM) in THF (2.4 mL) was added to a solution of ligand **L** (0.180 g, 0.61 mM) in THF (3.0 mL), what gave rise to the blue precipitate. The latter was dissolved by the addition of methanol (1.2 mL) and stirred for 24h at room temperature. The resulting complex was isolated by the crystallization using the slow diffusion of diisopropyl ether into THF/MeOH solution of complex. The crystals suitable for the single crystal X-

Ray crystallography and further studies were filtrated and washed with THF. Drying in the air gave blue crystals of complex **1** with yield of 52% (0.104 g, 0.16 mM).

FT-IR (KBr,  $\text{cm}^{-1}$ ):  $\nu(\text{O-H})$  3477;  $\nu(\text{N-H})$  3385, 3195;  $\nu(\text{C-H})_{\text{arom}}$  3160, 3053, 3032;  $\nu_{\text{as}}(\text{C-H})_{\text{alif}}$  2975, 2939;  $\nu_{\text{s}}(\text{C-H})_{\text{alif}}$  2898, 2841;  $\nu(\text{C=C})$  1627, 1555, 1521, 1471;  $\nu(\text{C=N})$  1442, 1392;  $\delta(\text{CH}_3)$  1353;  $\nu(\text{C-O})$  1262, 1219;  $\delta(\text{OCIO})$  1146, 1091;  $\gamma(\text{C-H})_{\text{arom}}$  1118, 1029, 1012, 957, 942, 836, 808, 781, 755, 721, 672, 637;  $\gamma(\text{ClO})$  626. ESI-MS(+)  $m/z$  (%): 188 (100)  $[\text{Cu}(\text{L-H})\text{K}_2(\text{CH}_3\text{OH})_2]^{3+}$ , 489 (10)  $[\text{CuL}(\text{CH}_3\text{OH})\text{Cl}]^+$ , 503 (9)  $[\text{CuL}(\text{CH}_3\text{OH})\text{OH}]^+$ , 521 (22)  $[\text{CuL}(\text{CH}_3\text{OH})_2\text{Cl}]^+$ , 535 (28)  $[\text{CuL}(\text{CH}_3\text{OH})_2\text{OH}]^+$ , 549 (18)  $[\text{CuL}(\text{CH}_3\text{OH})_3(\text{MeO})]^+$  Anal. calc. for  $[\text{Cu}(\text{C}_{17}\text{H}_{21}\text{N}_5\text{O}_4)(\text{CH}_3\text{OH})][\text{ClO}_4]_2$  (653.87) *The explosive nature of perchlorates prevents elemental analysis of the complex.*

### Synthesis of complex 2

A solution of copper(II) trifluoromethanesulfonate (0.137 g, 0.74 mM) in the absolute ethanol (1.0 mL) was added to the mixture of **A** (0.050 g, 0.37 mM) and **B** (0.073 g, 0.74 mM) in the absolute ethanol (2.0 mL). The clear blue solution was stirred for 24h at room temperature. The resulting complex was isolated by the crystallization using the diffusion of ethyl acetate into mother solution. The complex crystals suitable for the single crystal X-Ray crystallography and further studies were filtrated and washed with ethyl acetate. Drying in the air gave blue crystals of complex **2** with yield of 49% (0.138 g, 0.18 mM).

FT-IR (KBr,  $\text{cm}^{-1}$ ):  $\nu(\text{O-H})$  3507;  $\nu(\text{N-H})$  3247, 3198;  $\nu(\text{C-H})_{\text{arom}}$  3133, 3090, 3065;  $\nu_{\text{as}}(\text{C-H})_{\text{alif}}$  2988, 2946;  $\nu_{\text{s}}(\text{C-H})_{\text{alif}}$  2907;  $\nu(\text{C=C})$  1630, 1574, 1537, 1476;  $\nu(\text{C=N})$  1448, 1412;  $\delta(\text{CH}_3)$  1360;  $\nu_{\text{as}}(\text{SO}_3)$ ; 1340;  $\nu_{\text{as}}(\text{CF}_3)$  1281;  $\nu(\text{C-O})$  1258, 1228;  $\nu_{\text{s}}(\text{CF}_3)$ ; 1128;  $\nu_{\text{s}}(\text{SO}_3)$  1032;  $\gamma(\text{C-H})_{\text{arom}}$  1064, 1013, 969, 950, 905, 889, 840, 812, 786, 762, 728, 713, 639. ESI-MS(+)  $m/z$  (%): 278(100)  $[\text{CuL}(\text{H}_2\text{O})(\text{CH}_3\text{COOC}_2\text{H}_5)]^{2+}$ , 599 (89)  $[\text{CuL}(\text{H}_2\text{O})(\text{CH}_3\text{OH})_3\text{Cl}]^+$ , 553 (26)  $[\text{CuLCl}(\text{CH}_3\text{OH})(\text{H}_2\text{O})_2]^+$ ; Anal. calc. for  $[\text{Cu}(\text{C}_{19}\text{H}_{25}\text{N}_5\text{O}_4)(\text{H}_2\text{O})(\text{CF}_3\text{SO}_3)_2]$  (767.13); C, 32.88; H, 3.55; N, 9.13; found: % C, 32.29; H, 3.53; N, 8.98 %.

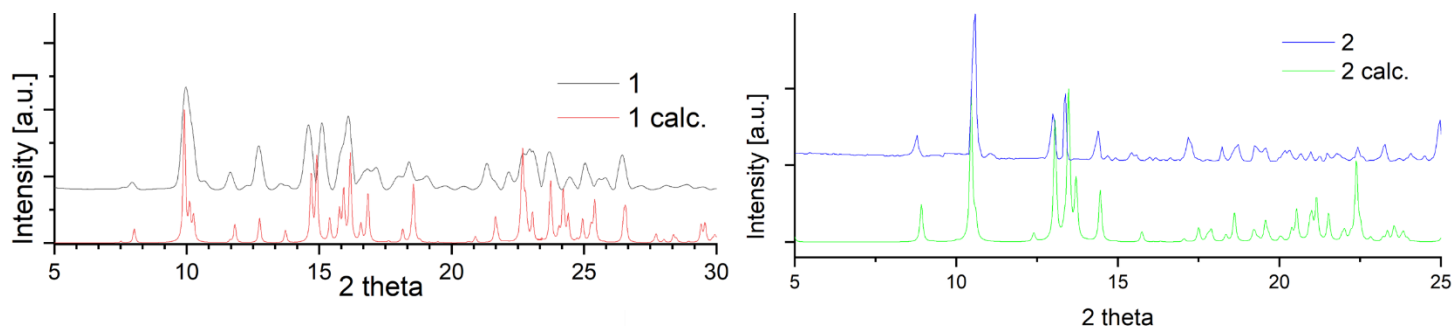


**Figure S1.** Experimental and simulated PXRD spectra of compounds **1** and **2**.

**Table S1.** Crystal data, data collection and structure refinement.

Compound	<b>1</b>	<b>1a</b>	<b>2</b>
Formula	$\text{C}_{18}\text{H}_{25}\text{CuN}_5\text{O}_5^{2+} \cdot 2\text{ClO}_4^-$	$\text{C}_{18}\text{H}_{25}\text{CuN}_5\text{O}_5^{2+} \cdot 2\text{ClO}_4^-$	$\text{C}_{19}\text{H}_{27}\text{CuN}_5\text{O}_5^{2+} \cdot 2\text{CF}_3\text{SO}_3^- \cdot \text{CH}_3\text{CH}_2\text{OH}$
Formula weight	653.87	653.87	813.20
Crystal system	triclinic	triclinic	triclinic
Space group	P-1	P-1	P-1
a(Å)	9.7716(4)	9.6287(4)	9.5535(7)
b(Å)	11.9652(4)	11.9833(5)	9.9440(6)
c(Å)	12.2930(6)	12.0249(5)	17.7730(11)
$\alpha$ (°)	80.798(3)	79.263(3)	92.720(5)
$\beta$ (°)	68.698(4)	68.067(4)	90.720(5)
$\gamma$ (°)	84.505(3)	83.306(4)	94.166(5)

V(Å <sup>3</sup> )	1320.75(10)	1262.84	1681.86(19)
Z	2	2	2
D <sub>x</sub> (g cm <sup>-3</sup> )	1.644	1.720	1.606
F(000)	670	670	834
μ(mm <sup>-1</sup> )	1.102	1.153	0.871
Reflections:			
collected	22490	12243	12543
unique (R <sub>int</sub> )	4658 (0.099)	5461 (0.235)	6737 (0.024)
with I>2σ(I)	4241	4874	6071
R(F) [I>2σ(I)]	0.1325	0.0298	0.0332
wR(F <sup>2</sup> ) [I>2σ(I)]	0.3081	0.0699	0.0797
R(F) [all data]	0.1377	0.0354	0.0379
wR(F <sup>2</sup> ) [all data]	0.3104	0.0731	0.0829
Goodness of fit	1.046	1.049	1.031
max/min Δρ (e·Å <sup>-3</sup> )	2.22/-1.13	0.41/-0.48	0.67/-0.46

**Table S2.** Relevant geometrical parameters (Å, °) with s.u.'s in parentheses. A and C are mean planes of terminal five-membered rings, B – of central pyridine ring.

	<b>1</b>	<b>1a</b>	<b>2</b>
Cu1-N2	1.964(8)	1.962(17)	1.9844(16)
Cu1-O7	2.489(8)	1.9689(16)	2.4475(15)
Cu1-N9	1.996(8)	2.0084(16)	2.0113(17)
Cu1-O14	2.388(7)	2.3452(13)	2.3783(14)
Cu1-N17	1.971(8)	1.9689(16)	1.9917(16)
Cu1-O1A (O1W)	1.955(9)	1.9852(14)	1.9405(14)
N2-Cu1-N17	178.0(4)	175.45(7)	174.86(7)
N9-Cu1-O1A	175.1(4)	172.63(6)	171.94(7)
O7-Cu1-O14	144.2(3)	144.29(5)	145.11(5)
A/B	73.9(4)	73.90(4)	72.82(7)
B/C	77.9(3)	77.91(3)	85.18(6)
A/C	76.11(5)	76.11(5)	74.47(7)

**Table S3.** Hydrogen bond data (Å, °).

D	H	A	D-H	H...A	D...A	D-H...A
<b>1</b>						
N6	H6	O4C	0.86	2.19	2.995(16)	156
N15	H15	O3B	0.86	2.21	2.956(16)	145
O1A	H1A	O18	0.93	2.52	3.040(13)	115
O1A	H1A	O2C <sup>i</sup>	0.93	2.44	3.27(3)	149
<b>1a</b>						

N6	H6	O4C	0.83	2.16	2.973(2)	168
N15	H15	O3B	0.88	2.15	2.919(2)	145
<b>2</b>						
N6	H6	O2B	0.88	2.25	3.056(2)	153
N15	H15	O1A	0.88	2.00	2.868(2)	168
O1W	H1W1	O1C	0.84	1.74	2.572(2)	171
O1W	H1W2	O3A <sup>ii</sup>	0.82	1.96	2.772(2)	170
O1C	H1C	O3B	0.84	1.94	2.778(2)	173

Symmetry codes: <sup>i</sup> x,1+y,z; <sup>ii</sup> 1-x,1-y,1-z.

**Table S4.** SHAPE analysis for 6-coordinated copper(II) complexes that exhibit slow relaxation of magnetization.

Shape (CN = 6)	Symmetry	1 (this work)	2 (this work)	Cu1 (2017 Boca et al.)	Cu2 (2017 Boca et al.)
Johnson pentagonal pyramid (J2)	C <sub>5v</sub>	25.757	24.185	24.838	23.257
Pentagonal pyramid	C <sub>5v</sub>	12.602	11.791	9.726	8.317
Octahedron	O <sub>h</sub>	<b><u>3.936</u></b>	<b><u>3.723</u></b>	<b><u>3.854</u></b>	<b><u>4.313</u></b>
Trigonal prism	D <sub>3h</sub>	23.172	21.386	21.168	19.593
Hexagon	D <sub>6h</sub>	31.769	30.212	33.833	32.288

**Table S5.** SHAPE analysis for **1** and **2** assuming coordination number 4 as a function of different square planar planes.

Shape (CN = 4)	Symmetry	1			2		
		N2-N9-N17- MeOH Plane	MeOH-N9-O7- O14 Plane	N2-N17- O7-O14 Plane	N2-N9- N17-H <sub>2</sub> O Plane	H <sub>2</sub> O-N9- O7-O14 Plane	N2-N17- O7-O14 Plane
Vacant trigonal bipyramid	C <sub>3v</sub>	32.758	28.151	22.294	30.056	28.284	22.795
Seesaw	C <sub>2v</sub>	17.949	18.756	11.376	15.472	18.750	11.456
Tetrahedron	T <sub>d</sub>	31.741	33.375	20.136	28.531	33.017	20.851
Square planar	D <sub>4h</sub>	<b><u>0.077</u></b>	<b><u>4.097</u></b>	<b><u>4.669</u></b>	<b><u>0.308</u></b>	<b><u>3.935</u></b>	<b><u>4.172</u></b>

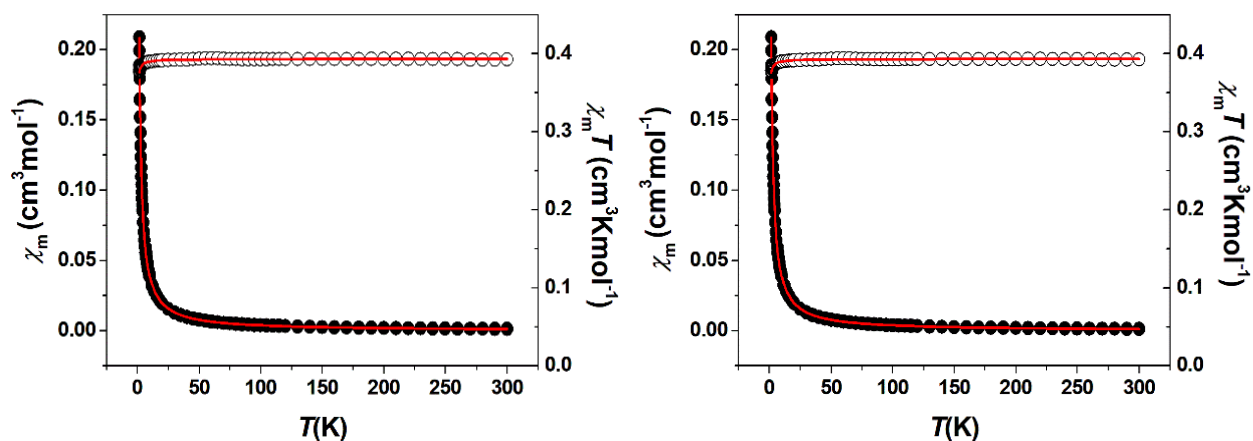


Figure S2. Temperature dependence of magnetic susceptibility and  $\chi_m T$  product of **1**(left) and **2** (right).

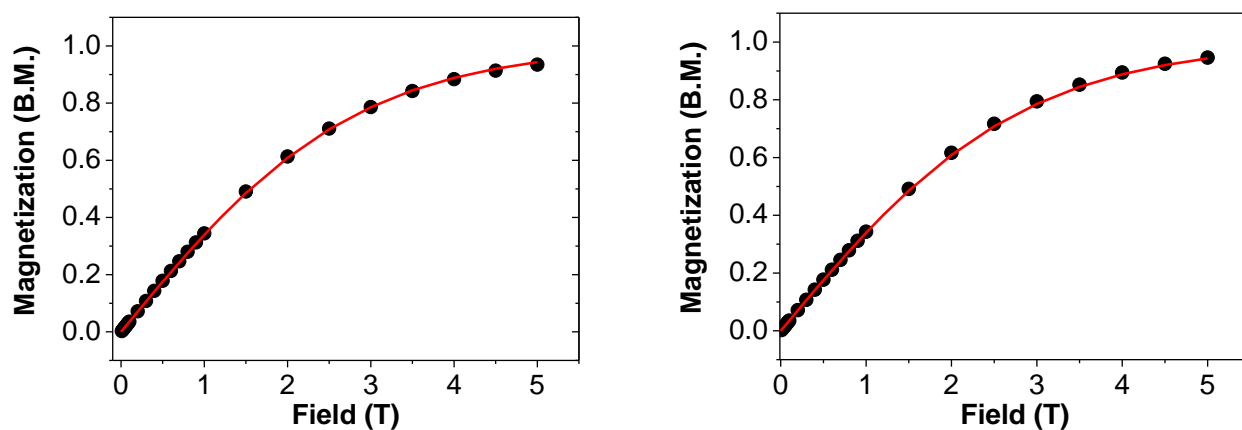


Figure S3. Magnetization versus magnetic field, measured at 2 K of both complexes, **1** (left), **2** (right). Solid red lines show theoretical Brillouin function for  $S = \frac{1}{2}$  and  $g = 2$ .

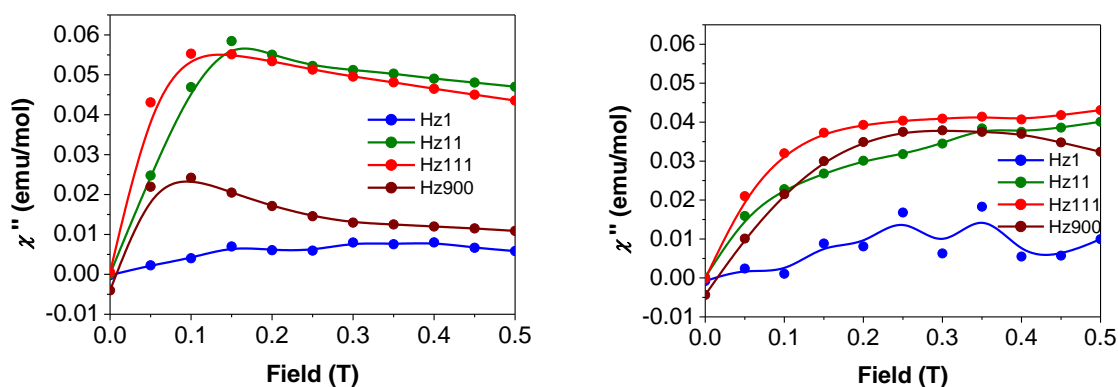
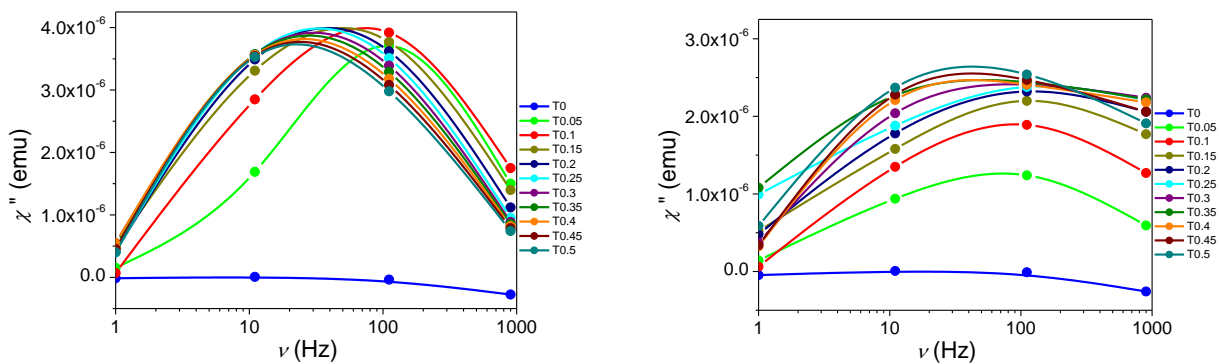
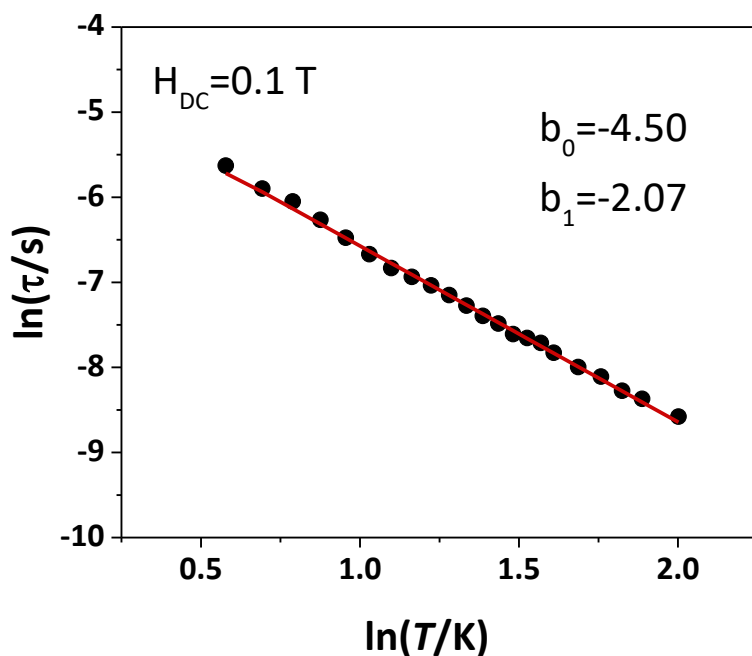


Figure S4. Out of phase susceptibility  $\chi''$  versus magnetic field relation for complexes **1**(left) and **2** (right).



**Figure S5.** Out of phase susceptibility  $\chi''$  versus magnetic field frequency relation for complexes **1** (left) and **2** (right).



**Figure S6.** Analysis of the relaxation time of **1**.

**Table S6.** Parameters from Debye<sup>54</sup> model of complex **1**.

	$T=1.8$ K	$T=2.4$ K	$T=3$ K	$T=3.6$ K	$T=4$ K	$T=4.6$ K
$\tau$	0.003968	0.001901	0.001079	0.000710	0.000557	0.000427
$\alpha$	<b>0.251853</b>	0.234399	0.213545	0.182279	0.198043	<b>0.160460</b>
$\chi_T$	0.229504	0.169299	0.133896	0.110691	0.099834	0.089990
$\chi_s$	0.015731	0.010726	0.085285	0.008126	0.007598	0.009630
$\mathbf{R}$	1.14E-04	1.56E-04	1.84E-04	2.24E-04	1.08E-04	1.25E-04

### III. CW-EPR

CW-EPR spectra were measured for the complexes **1** and **2** in the X- and Q-bands in the range from room temperature down to liquid nitrogen and helium temperatures, respectively. Changes of EPR spectra for **1** and **2** as a function of temperature are shown in Figure S7 and Figure S8, respectively and combined figure with representative temperatures (room, liquid nitrogen, liquid helium) are in Figure S9.

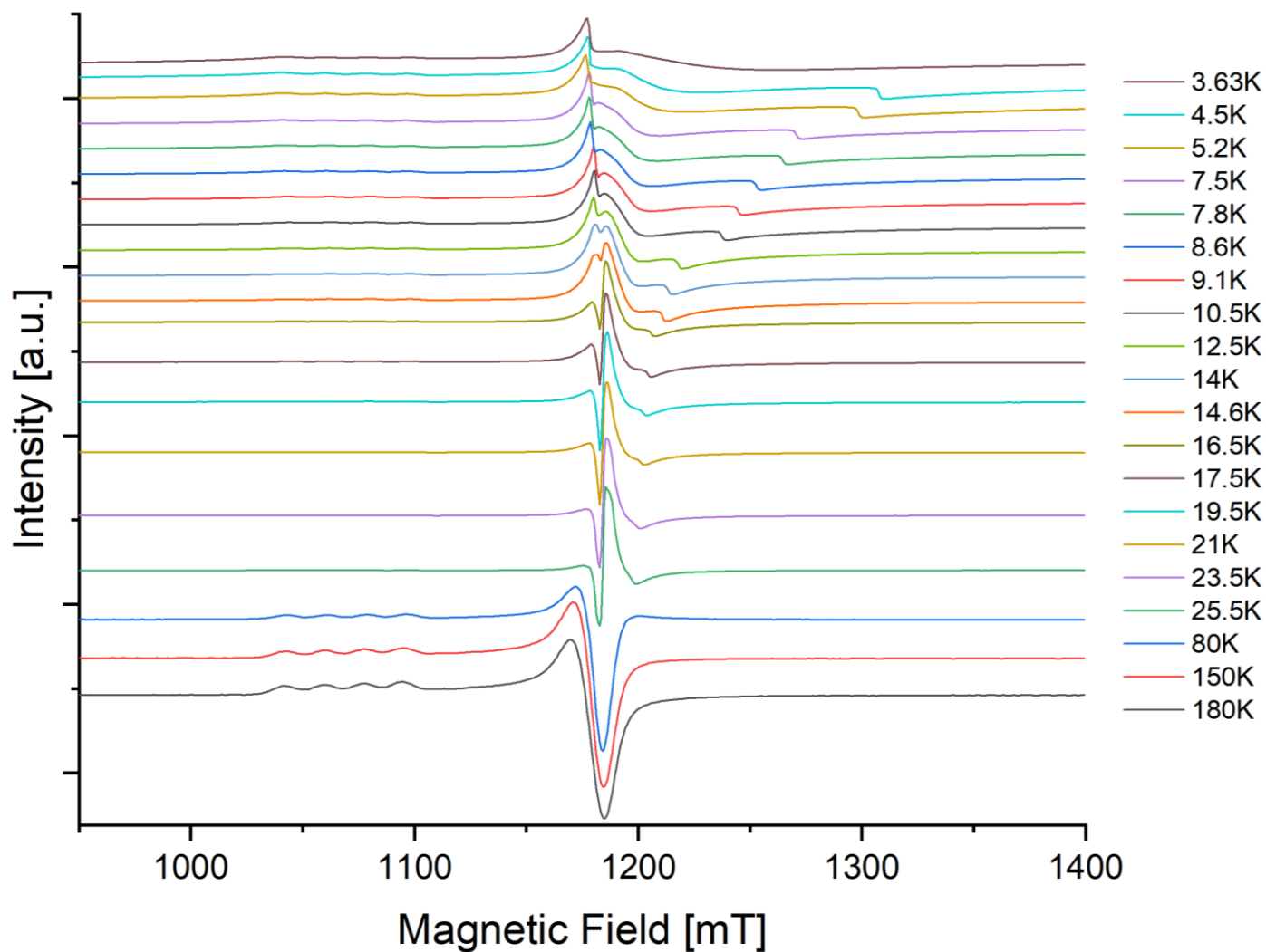


**Figure S7.** The temperature dependence of Q-band EPR spectra for complex **1**.

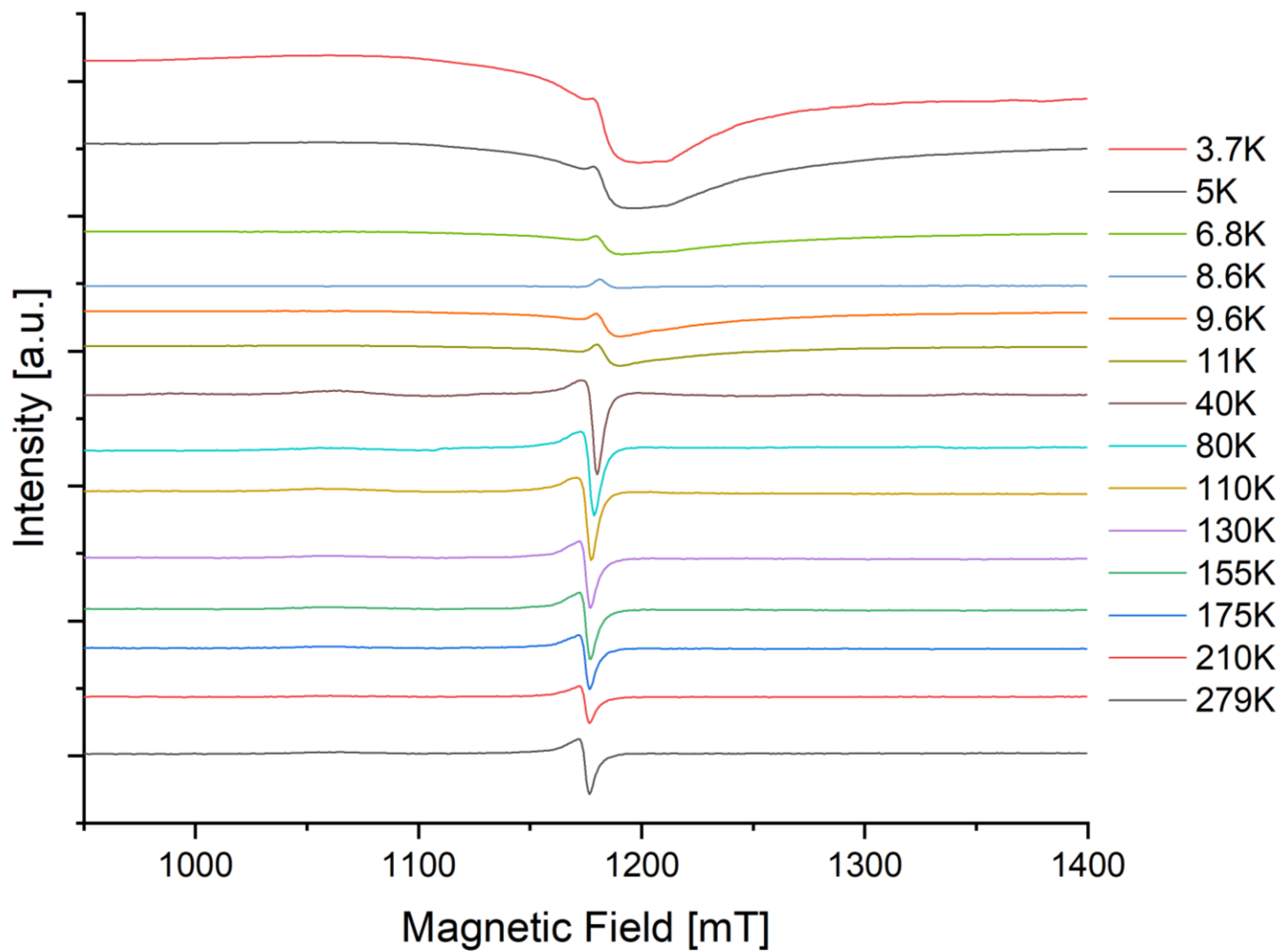


**Figure S8.** The temperature dependence of Q-band EPR spectra for complex 2.

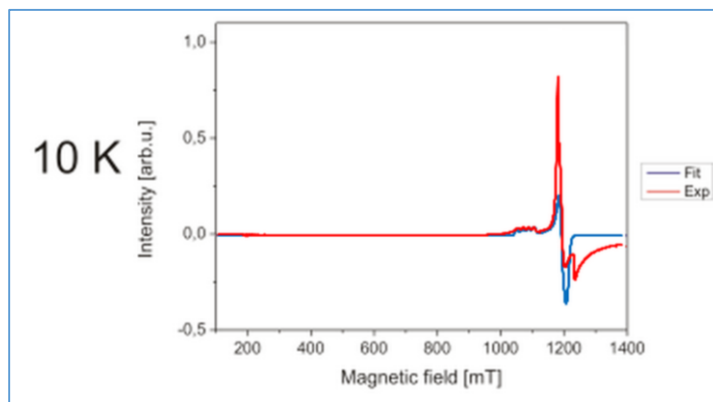
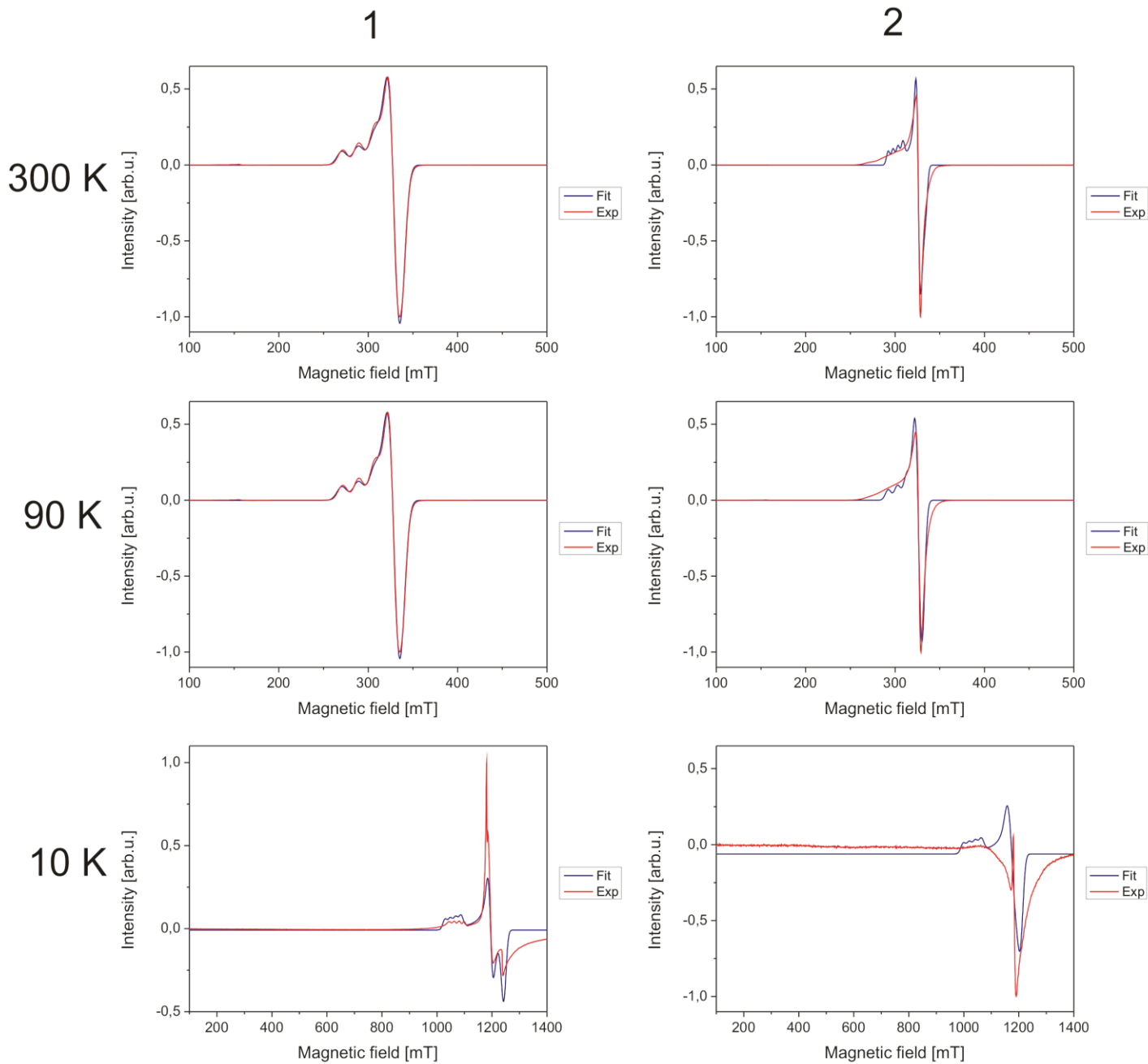


**Figure S9.** X-band (300K and 90K) and Q-band (10K) EPR spectra of **1** (a) and **2** (b) at 300K, 90K and 10K temperatures. Solid blue line shows simulated spectrum; for complex **2** simulations were based on the use of one component only. Simulation for **1** (Q-band, 10K) was also performed with fixed parameter  $g_1 = 2.000$  and monomodal peak distribution (blue frame).

Sample superimposed EPR spectra obtained at 300 K for **1** and **2** are shown in Figure S10. These spectra enabled to determine the EPR line parameters, i.e. the resonance field, line width  $B_{pp}$ , and the EPR line intensity. Figure S11 shows the temperature dependence of EPR line width  $B_{pp}$  for both compounds. Analysis of the temperature dependence of the width and intensity of EPR line (Figures S10 and S11) has enabled to estimate the total intensity of the EPR line ( $I_{EPR}$ ) using the relation:  $\Delta B_{pp}^2 * I_{EPR}$ , since this quantity is proportional to the area under the absorption curve. Figure S12 shows the reciprocal dependence of the total EPR spectral intensity as a function of temperature down to liquid nitrogen regime.

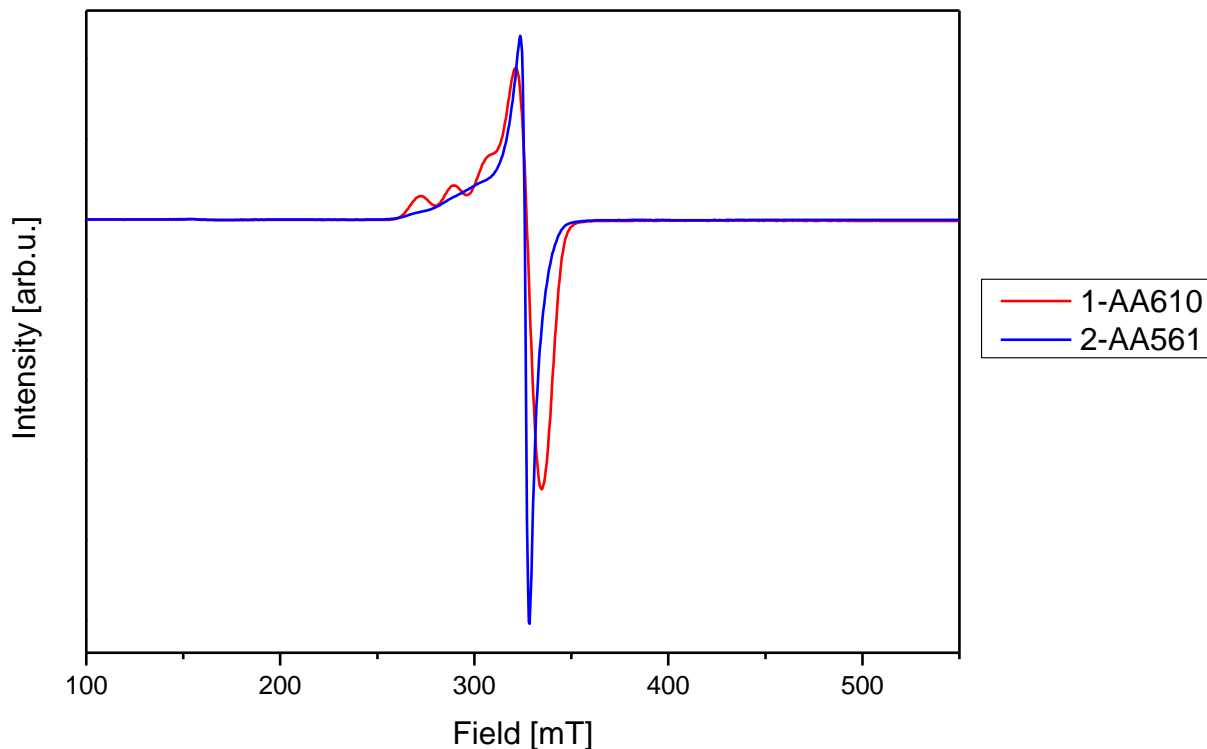


**Figure S10.** X-band EPR spectra for the Cu(II) ion in complexes **1** (red) and **2** (blue) at 300 K.

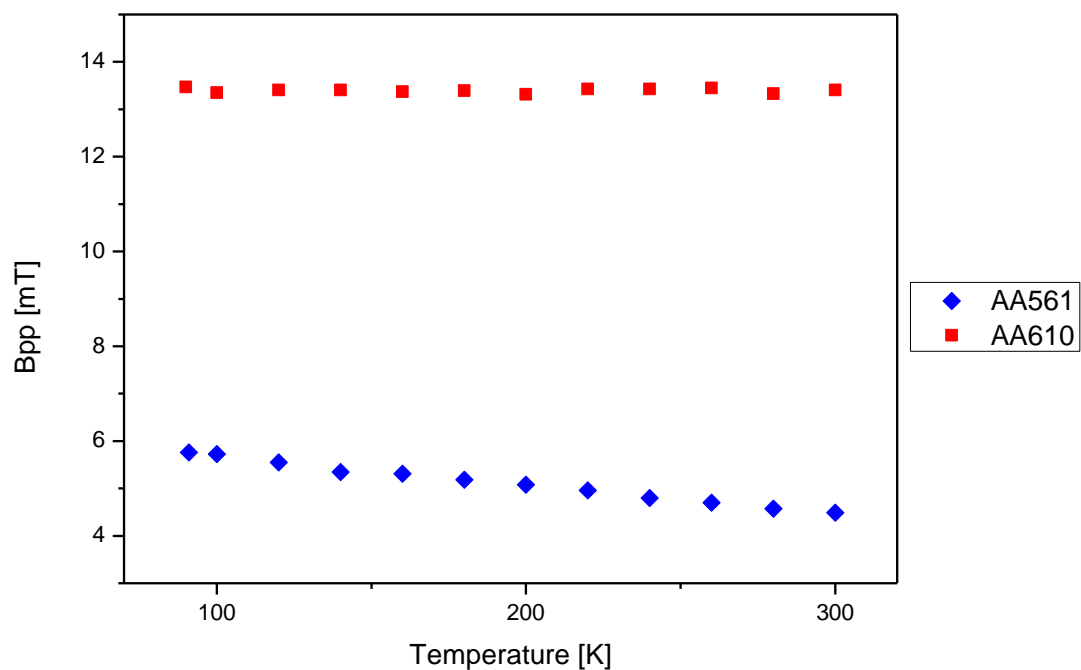


**Figure S11.** The line width  $B_{pp}$  the EPR lines for complexes **1** (red) and **2** (blue).

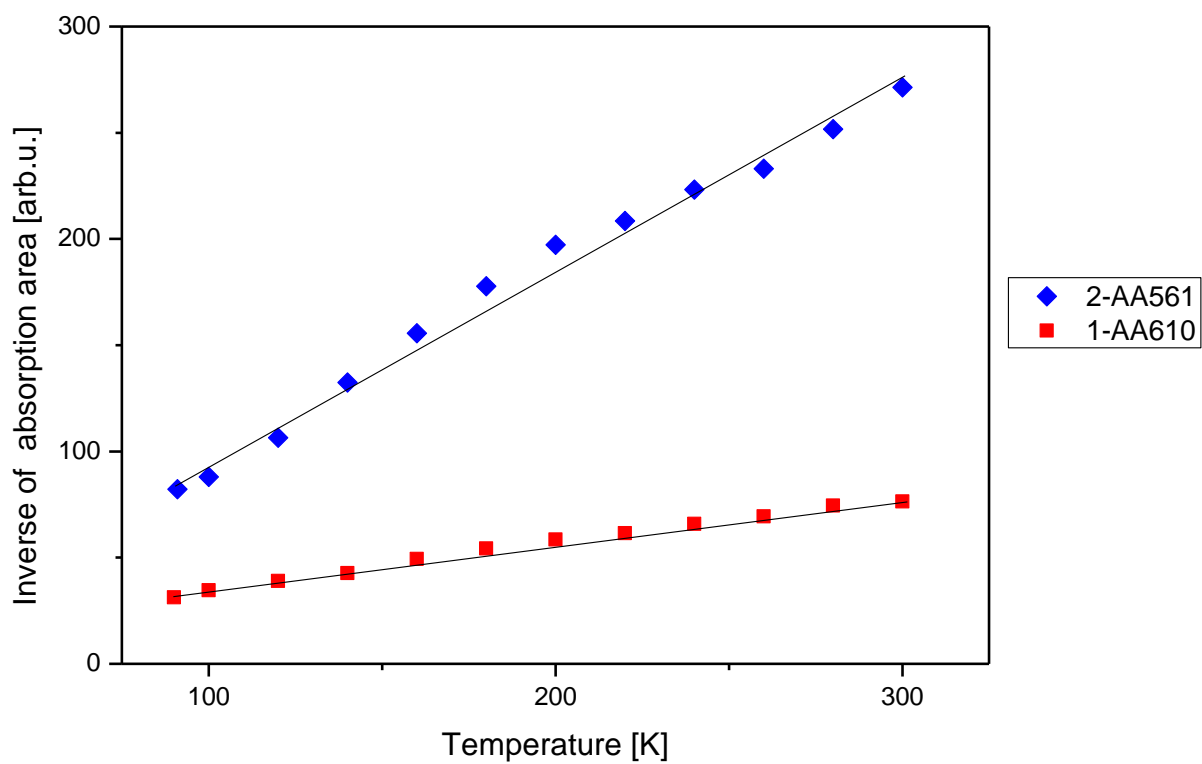


**Figure S12.** Temperature dependence of the inverse total EPR line intensity on the for complexes **1** and **2**.

It appears that the data in Figure S12 are characteristic for the linear behavior predicted by the Curie law for slightly exchange coupled ferromagnetic systems.<sup>55</sup> However, the interpretation invoking exchange interactions between Cu(II) ions may be excluded based on the following arguments.

- (1) The interatomic distances between Cu(II) ions in complexes **1** and **2** are quite large, ranging from 0.8 - 0.95 nm, moreover no suitable pathway for exchange interactions between neighboring Cu ions can be identified.
- (2) The magnetic susceptibility studies (see Sections 2.4 and 2.5) indicate absence of exchange interactions.
- (3) The EPR spectra observed by us for complex **1** are identical to the spectra from isolated paramagnetic centers.

For complex **2** a slight broadening of EPR lines at very low temperatures is observed, which may be ascribed either to very weak exchange interactions between Cu(II) ions or other factors. In any case, the above finding indicate that magnetic interactions are negligible in complex **2**, whereas the observed broadening is discernible only due to the high sensitivity of the EPR method.

For complex **2** EPR spectra were first fitted using single center approach, i.e. taking into account separately one of the two discernible spectral components: A and B. These results are shown in Figure S13 (300 K) and Figure S14 (91 K). In view of the lack of satisfactory agreement, next we have considered combined simulations of both spectral components. The existence of two centers in complex **2** is plausible based on the crystallographic structure. Figure S1 reveals two Cu(II) complexes in the unit cell, which are crystallographically equivalent but magnetically inequivalent being oriented in an antiparallel way. The composite spectra obtained for complex **2** using two spectral components A and B arising from the two centers are shown in Figure S15 (300 K) and Figure S16 (91 K).

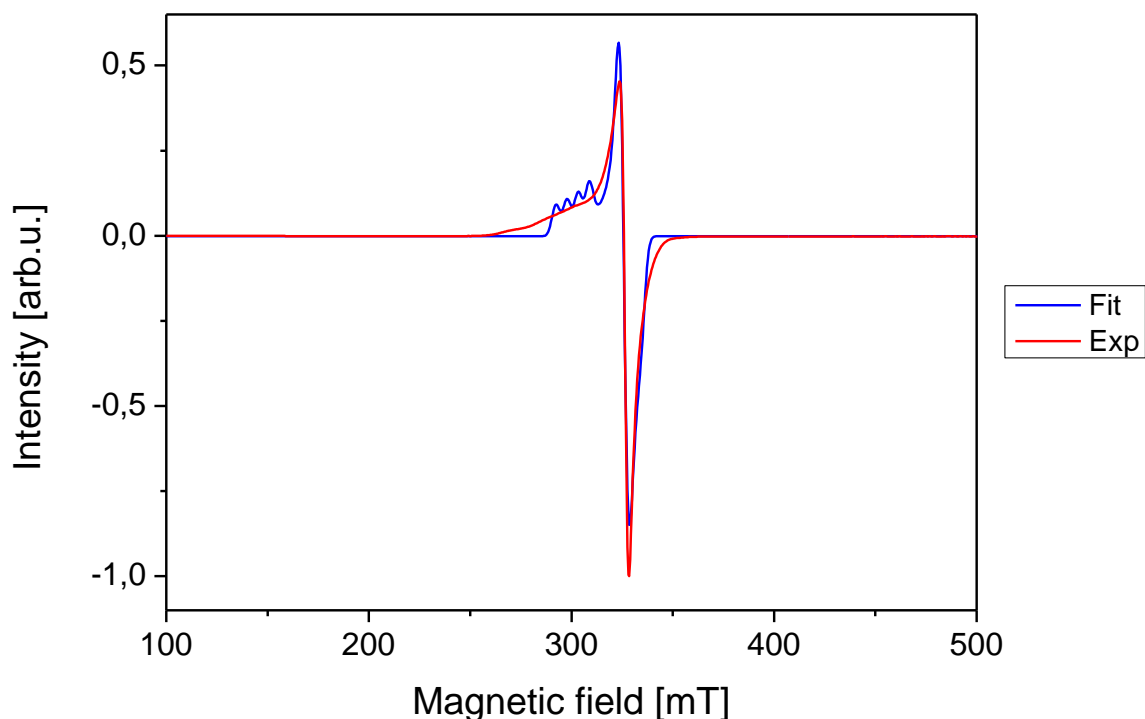


**Figure S13.** Experimental (exp) and fitted (fit) EPR spectrum using one spectral component only for complex **2** at 300 K.

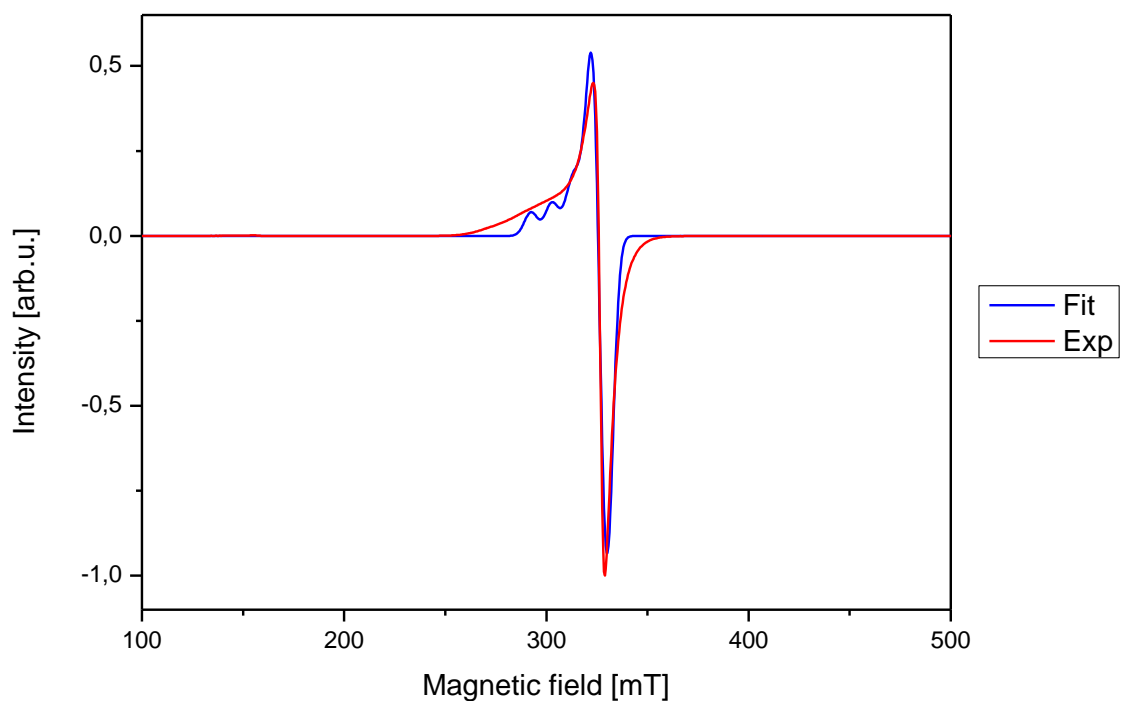


**Figure S14.** Experimental (exp) and fitted (fit) EPR spectrum using one spectral component only for complex **2** at 91 K.

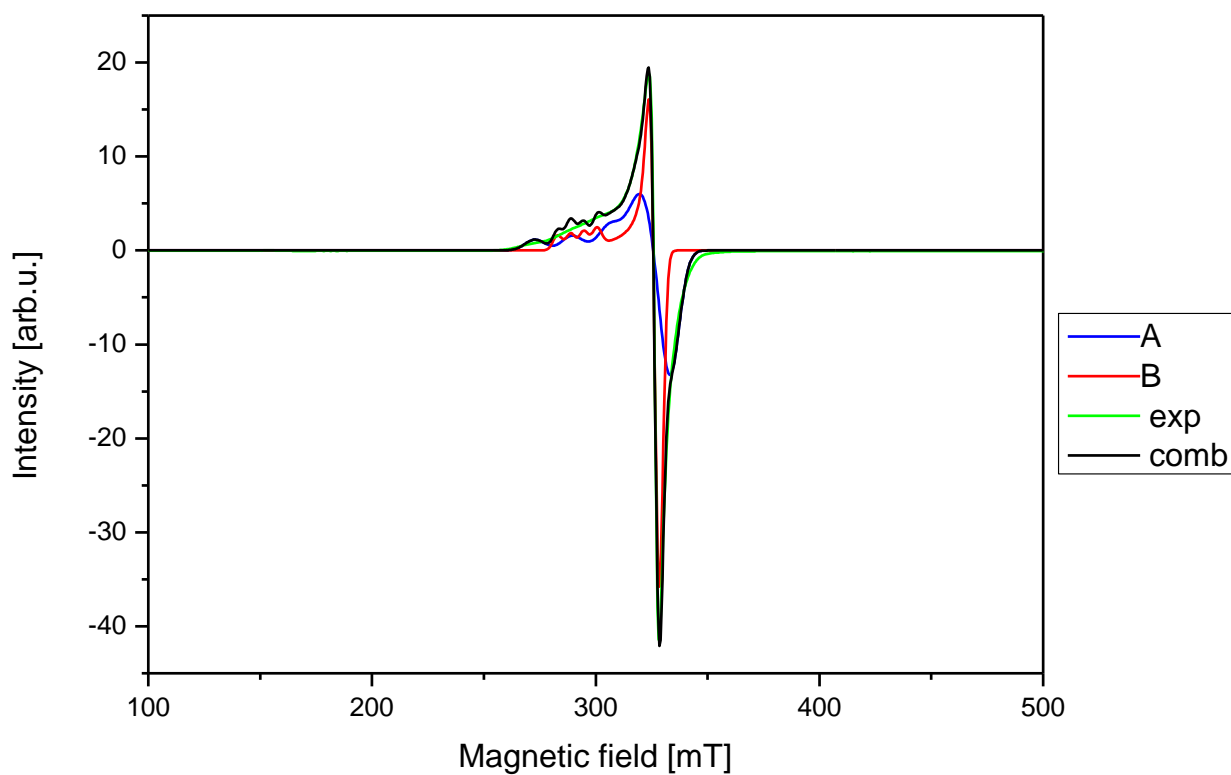


**Figure S15.** Experimental (exp) EPR spectrum for complex **2** and spectra simulated using: (i) simulations of separate lines (A, B) and (ii) combined simulations of both spectral components (comb) at 300 K.

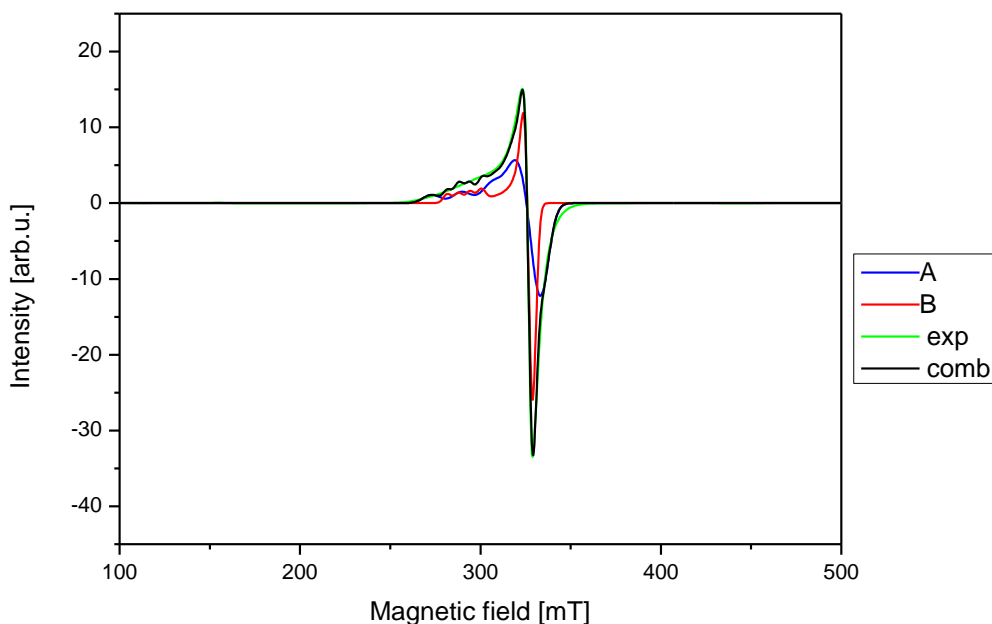


**Figure S16.** Experimental (exp) EPR spectrum for complex **2** and spectra simulated using: (i) simulations of separate lines (A,B) and (ii) combined simulations of both spectral components (comb) at 91 K.

Initially, we have encountered problems with interpretation of the temperature dependence of cw-EPR. Basically, there is almost no change from room temperature to around 30 K for complex **2** (Figure S8). Then, below 30 K we observe changes in the shape of the spectra, which can be due to the appearance of two slightly distinct components. Interestingly, one component is almost unchanged below 30 K, while the other component undergoes significant changes. Below 10 K the changes of EPR spectra (see, Figure S7 - complex **1** and Figure S8 - for complex **2**) are so large that their meaningful interpretation pose problems. For complex **2** these problems may be solved by using two components, which results in a much better matching of the simulated spectra and the experimental EPR spectrum (Figures S15 and S16). A more meaningful interpretation of these changes would require other complementary measurements, which are beyond the scope of this study. Note that also for complex **1** the spectra may be considered as due to two components, but both components would appear the same above 30 K, whereas below 30 K one component undergoes some changes.

From the EPR data down to liquid nitrogen temperatures, it can be concluded that the perceived magnetization associated to the paramagnetic centers in both compounds is negligible and thus follows a Curie-like behavior (compare with magnetic studies Sections 2.4 and 2.5). This indicates that EPR spectra can be ascribed to isolated paramagnetic centers in complexes **1** and **2**. This finding means that exchange interactions, which could be acting in complexes **1** and **2**, are indeed very weak and incapable to produce long-range magnetization effects. Nevertheless, such negligible exchange interactions may be strong enough to induce coalescence of lines and thus broadening of the spectra due to the hyperfine interactions.

For both complexes **1** and **2**, calculations of energy levels were performed using EasySpin program<sup>4,5</sup> for the parallel (z) and perpendicular (xy) directions of the static magnetic field  $B_0$ . Figures S17 and S18 show the energy levels as well as microwave-induced transitions and their probabilities calculated using the fitted SH parameters in Table 1 for 300 K. The figures illustrate the possible transitions between the states of the electronic spin ( $S = 1/2$ ) and nuclear spin ( $I = 3/2$ ) observable in our EPR studies and confirm the compliance with the observed spectra.  $\perp$ ). Transition energy levels at the resonance field  $B_{res}$  are presented in Tables S7 and S8.

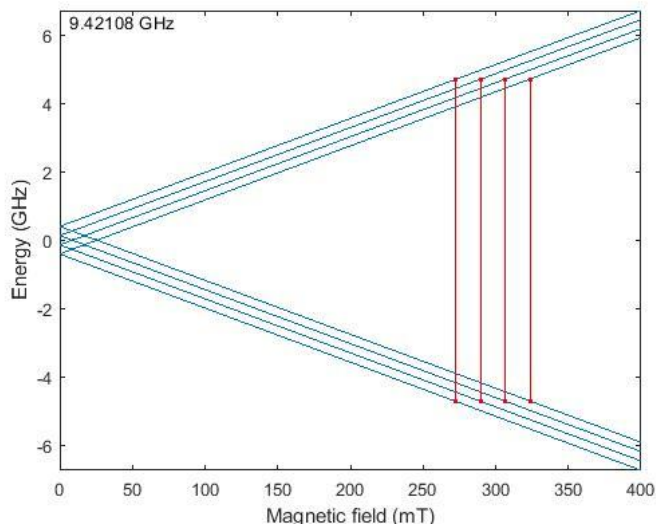


**Figure S17.** Energy levels for complex **1** at resonance frequency 9.42108 GHz with  $B_0 \parallel z$ . Red lines show all possible transitions with probability equal 1 generated automatically by EasySpin program.

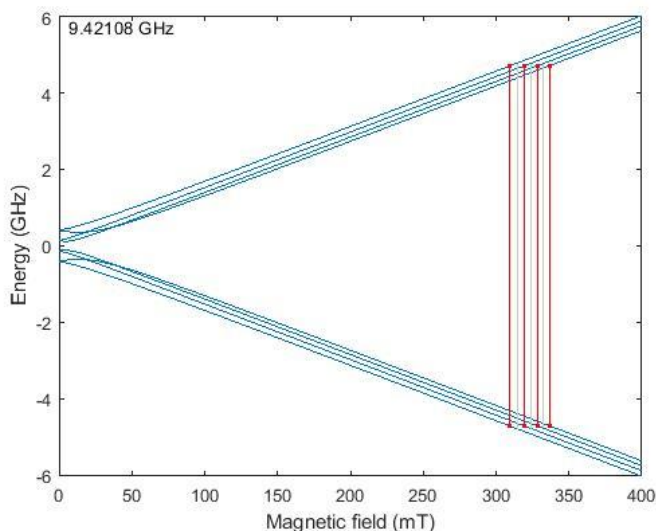


**Figure S18.** Energy levels for complex **1** at resonance frequency 9.42108GHz with  $B_0$  in the xy-plane. Red lines show all possible transitions with probability from 0.98 to 1.0, blue lines - with probability from 0.0015 to 0.0026 generated automatically by EasySpin program.

**Table S7.** Energy levels (ELs, in GHz) associated with the transitions at the resonance field ( $B_{res}$ ) indicated in Figures S17 and S18 for complexes **1** and **2**.

	complex 1			complex 1			complex 2			complex 2		
Temp [K]	300			180			300			300		
Band	X			Q			X			Q		
Orientation	$B_{res}$	Lower ELs	Upper ELs									
	[mT]	GHz	GHz									
$B_0 \parallel z$	272.4	-4.715	4.706	1042.9	-16.913	16.878	272.3	-4.715	4.705	1026.8	-16.914	16.879
	289.4	-4.712	4.709	1060.5	-16.901	16.889	284.2	-4.712	4.708	1040	-16.903	16.891
	306.5	-4.709	4.712	1077.9	-16.889	16.902	296.0	-4.708	4.712	1053.2	-16.891	16.903
	323.5	-4.705	4.716	1095.5	-16.877	16.914	307.9	-4.705	4.715	1066.3	-16.879	16.915

$B_{0  }(x,y)$	309.6	-4.713	4.708	1140.1	-16.905	16.886	308.3	-4.712	4.708	1135.4	-16.905	16.888
	319.4	-4.711	4.71	1149.5	-16.899	16.892	315.1	-4.711	4.709	1142.6	-16.900	16.894
	328.5	-4.71	4.711	1158.7	-16.892	16.899	321.5	-4.709	4.711	1149.8	-16.894	16.900
	336.7	-4.708	4.713	1167.6	-16.886	16.905	327.5	-4.708	4.712	1156.7	-16.888	16.905

**Table S8.** Energy levels (ELs, in GHz) associated with the transitions at the resonance field ( $B_{res}$ ) indicated in Figures S17 and S18 for complex **2** and two components A and B.

Component A				Component B			
$B_{res}$	Orientation	Lower ELs	Upper ELs	$B_{res}$	Orientation	Lower ELs	Upper ELs
[mT]		GHz	GHz	[mT]		GHz	GHz
273.6	$B_{0  z}$	-4.715	4.705	284	$B_{0  z}$	-4.715	4.705
289.8		-4.712	4.708	289.7		-4.712	4.708
306.0		-4.708	4.712	295.5		-4.708	4.712
322.3		-4.704	4.716	301.3		-4.705	4.715
307.4	$B_{0  }(x,y)$	-4.713	4.707	317.7	$B_{0  }(x,y)$	-4.711	4.709
316.6		-4.711	4.709	320.8		-4.709	4.711
325.1		-4.709	4.711	323.8		-4.708	4.713
332.9		-4.707	4.713	324.6		-4.712	4.708

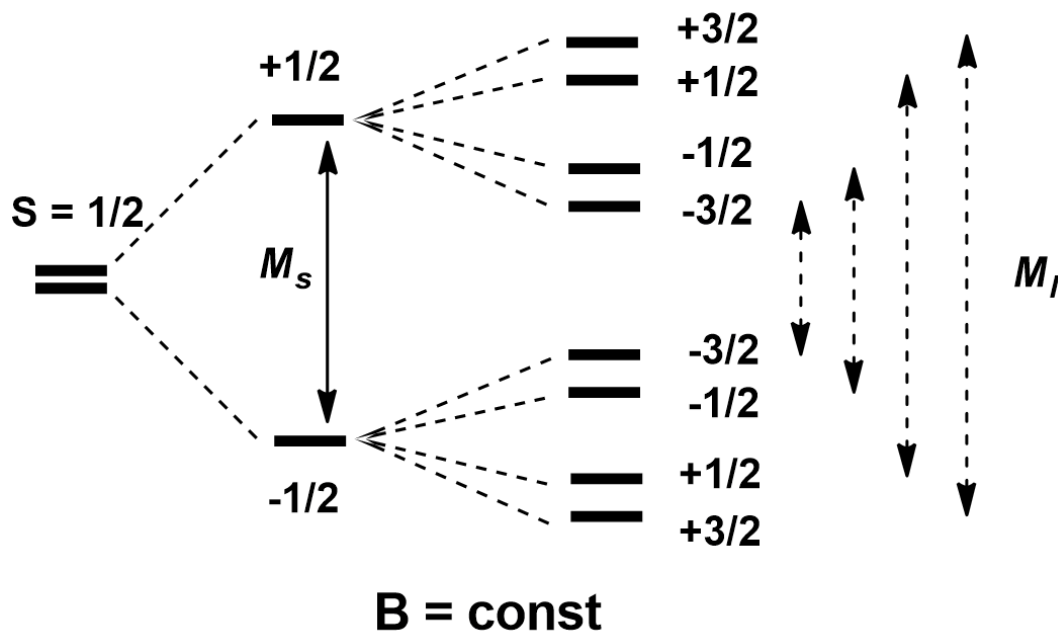
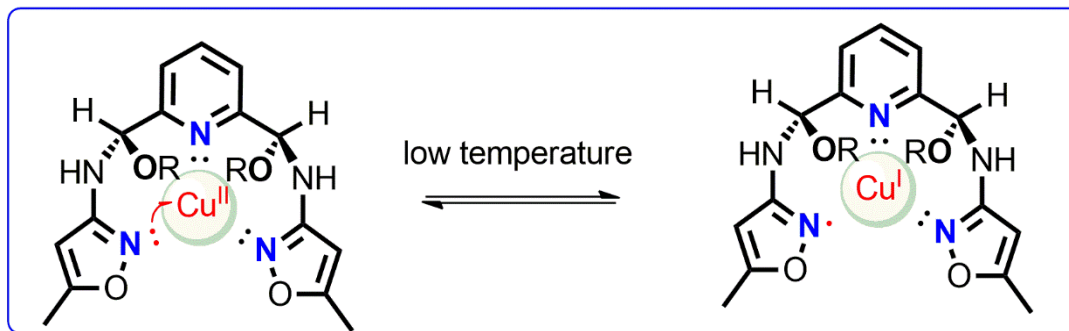
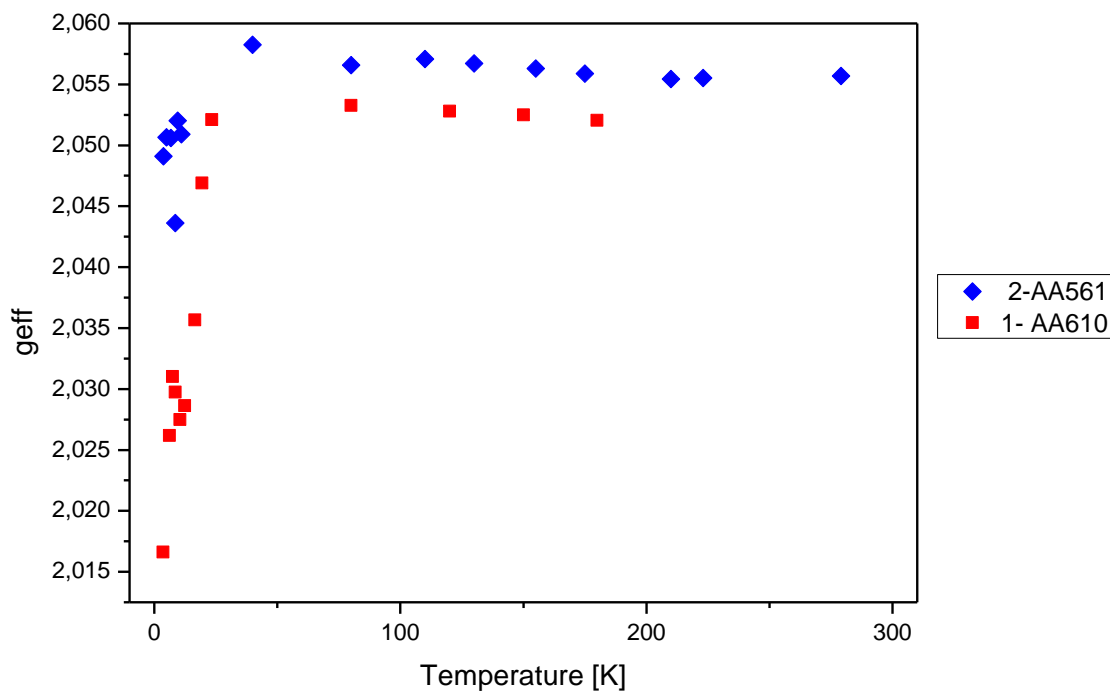


**Figure S19.** Hyperfine energy levels of Cu(II) ions in a coordination compound with allowed transitions indicated.

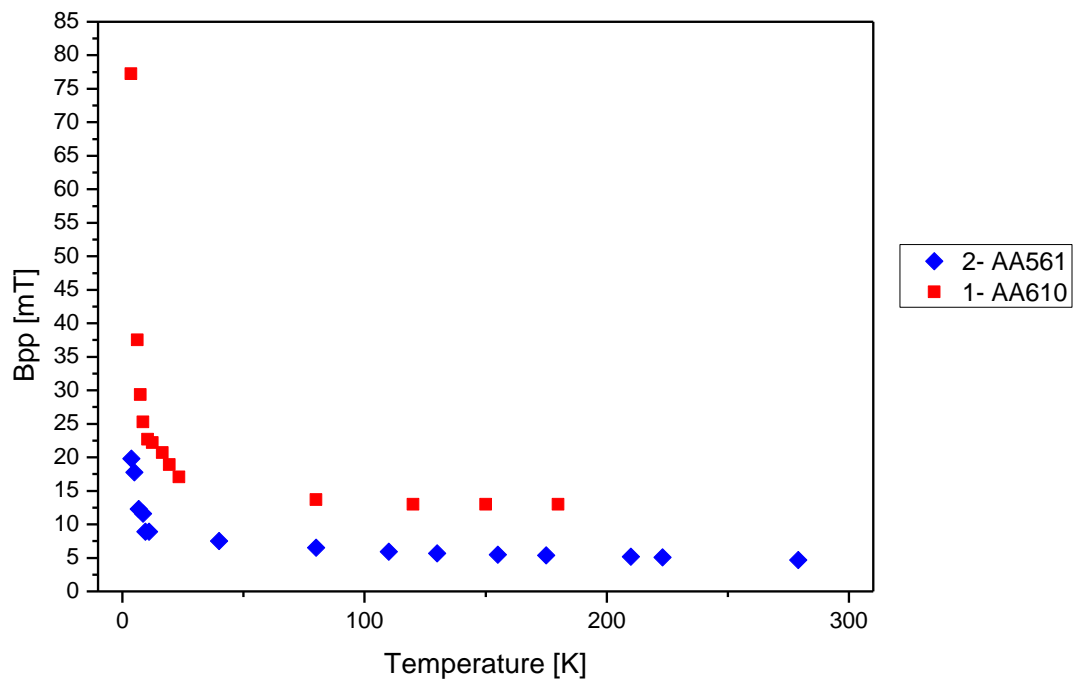


**Scheme S1.** Graphical representation of the origin of the presumed Cu(I)NO nitrosyl-related radicals. Coordinated solvent molecule and counterions are omitted for clarity.

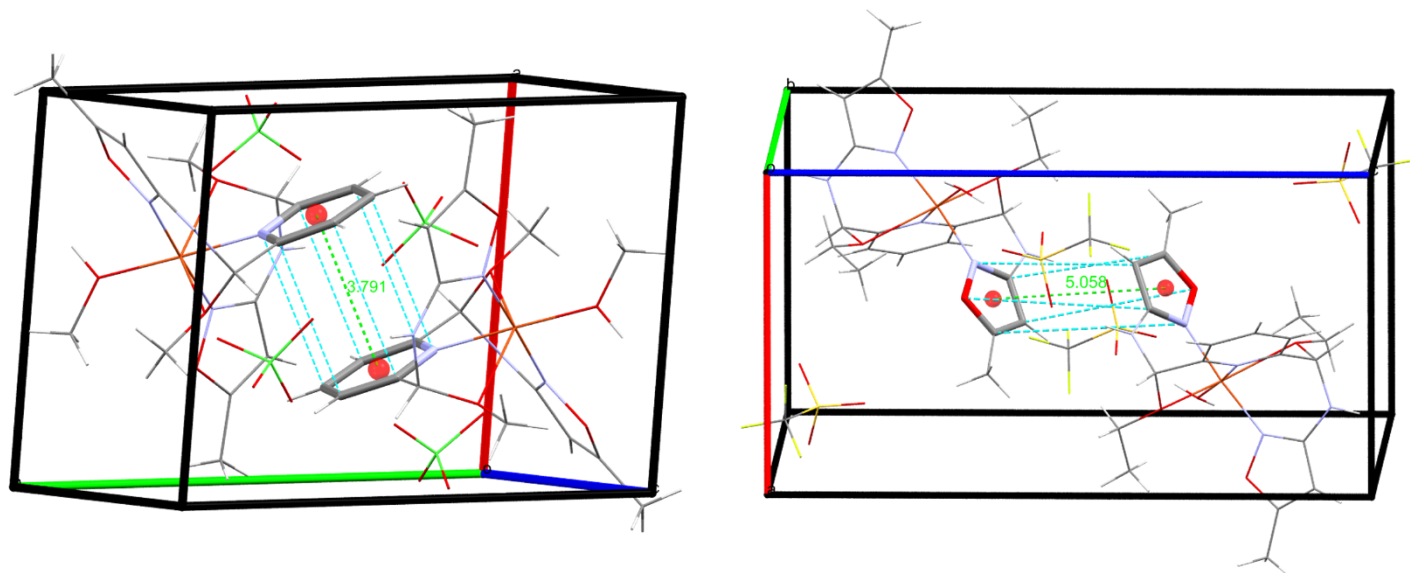
CW EPR measurements enabled to determine the temperature dependence of the  $g_{eff}$  factor (Figure S21) and the EPR line width  $B_{pp}$  (Figure S22) for both compounds down to liquid helium temperature.



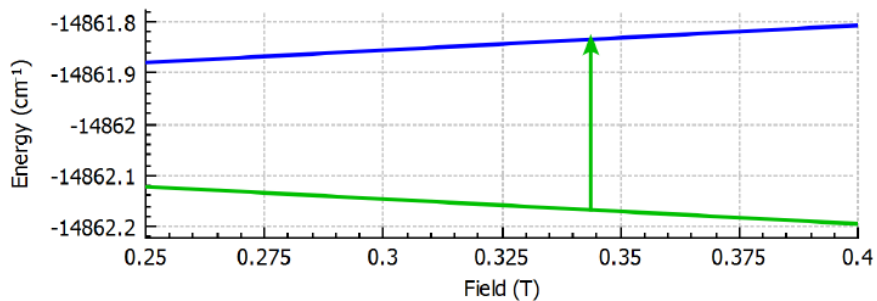
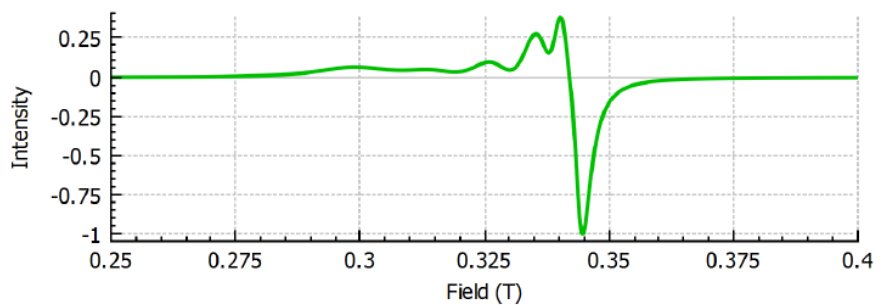
**Figure S20.** Temperature dependence of the  $g_{eff}$  factor for complexes **1** and **2**.



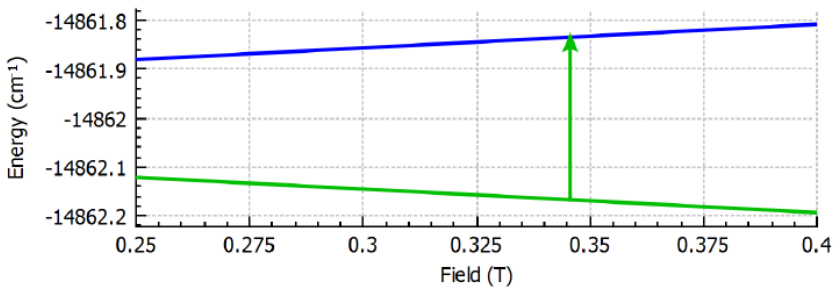
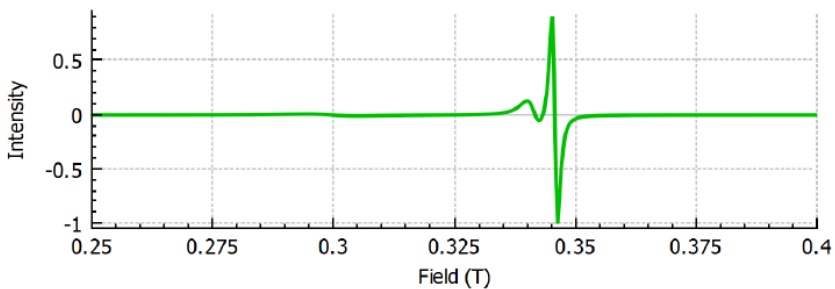
**Figure S21.** Temperature dependence of the line width  $B_{pp}$  for the complexes **1** and **2**.



**Figure S22.** X-ray graphical representations of crystallographically equivalent but magnetically inequivalent Cu(II) pairs of **1** and **2**.



**Figure S23.** The averaged EPR powder spectrum obtained from PHI simulations using integration over several directions of magnetic field, for linewidth equal to 0.1 GHz, 0.15 GHz, 0.6 GHz along the x-, y-, z-axis, respectively. The indicated transition corresponds to the magnetic field directed along the x direction.



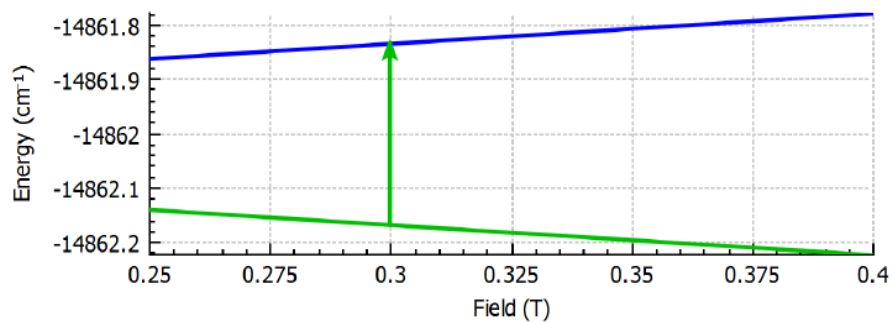
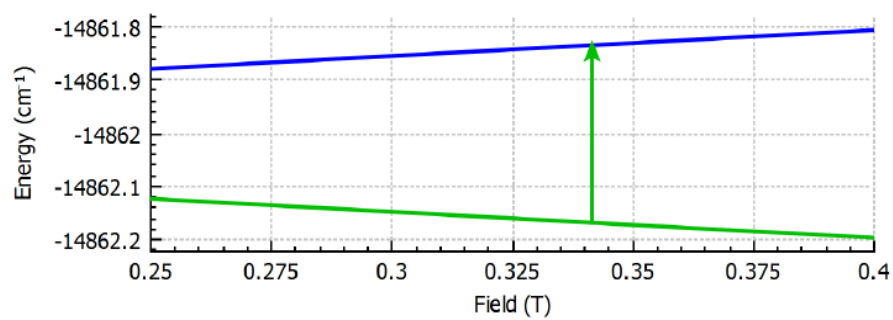


**Figure S24.** EPR spectrum obtained from PHI simulations using integration over three main directions of magnetic field, for linewidth equal to 0.05 GHz, 0.15 GHz, 0.6 GHz along the x-, y-, z-axis, respectively. The indicated transitions correspond from upper to lower to the magnetic field directed along the x-, y-, and z direction, respectively.

#### IV. Optical spectroscopy

The nearest surrounding of Cu(II) ion in **1** is formed by 3 N atoms and 3 O atoms and the actual site symmetry of Cu(II) center is  $C_1$ . The Figure S29 shows, that appropriate selection of (x, y, z) axis system (see Section IV and Table S9) allows to approximate the actual symmetry with  $C_2$  symmetry. The axis system (x, y, z) was selected with the origin (0, 0, 0) on the Cu atom, the oxygen atom O1A on the z axis, the N2 and N17 atoms almost exactly on the x axis (angle  $\theta = 90.60^\circ$ ). The coordination polyhedron of Cu(II) ion can be also considered as a distorted octahedron (Sections 2.2 and 2.3). The major deviation from the ideal octahedron results from position of O7 and O14 atoms. The angles O7-Cu-O1A and O14-Cu-O1A are  $111.13^\circ$  and  $104.56^\circ$ , respectively, and the angles O14-Cu-N2 and O7-Cu-N17 are  $99.92^\circ$  and  $97.12^\circ$ , respectively, whereas for perfect octahedron all angles should be equal to  $90^\circ$ . Moreover, the Cu-O14 and Cu-O7 distances (238.8 and 248.9 ppm) are larger than distances between Cu and other atoms, which are very similar and confined within 195.6 pm (Cu-O1a) - 199.6 pm (Cu-N9) range. This is also corroborated by the SHAPE calculations from the analysis of the deviations from the square planar planes. From the three planes that can be constructed from the octahedral geometry by elimination of axial ligands, the highest S value corresponds to the N2-N17-O7-O14 planes, both for complexes **1** and **2** (Tables S4 and S5).

Comparison of deviation between **1** and **2** in this plane is higher for **1** (4.669 vs 4.172) and this falls in line with the results of magnetic studies *i.e.* that slow magnetic relaxation for the triflate analogue **2** is much faster than in the case of **1**. In addition, the deviation of the N2-N9-N17-MeOH/H<sub>2</sub>O planes is also higher and should contribute to the observed magnetic phenomena. Nevertheless, in spite of this deviation the use of the symmetry descent scheme  $O_h \rightarrow D_{4h} \rightarrow C_2$  for rationalization of absorption spectrum of **1** is fully justified (Fig.6bottom). In the hole formalism the degenerate  $5d$  levels of  $3d^9$  configuration of Cu(II) are split by an  $O_h$  field into a double degenerate  ${}^2E_g$  and a triply degenerate  ${}^2T_{2g}$  states. A tetragonal distortion splits  ${}^2E_g$  into  ${}^2B_{1g}(dx^2-y^2)$  and  ${}^2A_{1g}(dz^2)$ , whereas  ${}^2T_{2g}$  into an orbital singlet  ${}^2B_{2g}(dxy)$  and a doublet  ${}^2E_g(dxy, dy, z)$ .<sup>56</sup> The tetragonal distortion may lead to shortening or lengthening of the axial Cu-ligand bonds. In the first case the lowest energy level is  ${}^2B_{1g}(dx^2-y^2)$  and the following relation between  $g$  values determined from EPR spectra are expected:  $g_{\parallel} > g_{\perp} > g_e$ . Shortening of the axial Cu-ligand bond corresponds to the  ${}^2A_{1g}(dz^2)$  ground level and EPR spectra are then characterized by  $g_{\perp} > g_{\parallel} = g_e$ .<sup>57-60</sup> In our case the  $g$ -values obtained from EPR are  $g_{\parallel} = 2.26$  and  $g_{\perp} = 2.05$  and this indicates that the ground level would be  $dx^2-y^2$  at the tetragonal approximation. The lowering of symmetry from tetragonal to  $C_2$  leads to transformation of  ${}^2B_{1g}$ ,  ${}^2A_{1g}$  and  ${}^2B_{2g}$  into  ${}^2A$  states, and the doublet  ${}^2E_g$  is splits into two  ${}^2B$  single states (Figure 6bottom). Moreover, for symmetry as low as  $C_2$  a significant mixing is expected between  ${}^2A$  states originating from  ${}^2E_g(O_h)$  as well as between  ${}^2B$  states originating from  ${}^2T_{2g}(O_h)$  (Figure 6bottom). Accordingly, the lowest state is expected to be a mixed  $dx^2-y^2$  and  $dz^2$  state. An alternative interpretation could assume that the splitting of the levels arising from  $E_g(O_h)$  is small. The absorption spectrum was measured starting from  $4000\text{ cm}^{-1}$  and no band was observed in the energy range  $4000 - 12,000\text{ cm}^{-1}$ . Hence the energy difference between the two lowest levels  ${}^2A(E_g)$  would have to be smaller than  $4000\text{ cm}^{-1}$ . Then the bands observed in the absorption spectrum would be associated with transitions to 3 levels arising from  $T_{2g}(O_h)$ . Figure S27 shows deconvolution of the spectrum into 3 bands obtained according to this assumption based on interpretation II. Matching the calculated and experimental spectrum is slightly worse than in the case of deconvolution into 4 bands in the inset of Figure 6. Assuming this alternative structure of energy levels and that the center of gravity of levels  $A(E_g)$  is below  $2000\text{ cm}^{-1}$ , then  $Dq$  can be estimated as  $\sim 1285\text{ cm}^{-1}$ .

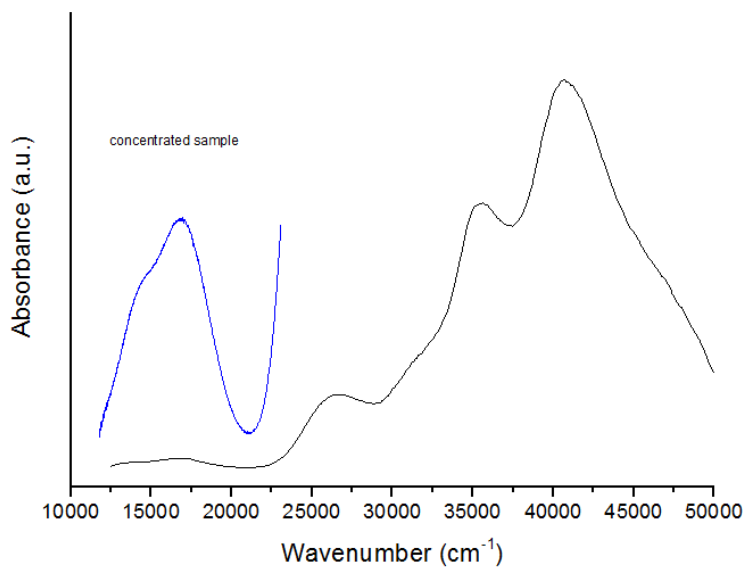


**Figure S25.** Absorption spectrum for the thin film of **1** measured at RT.

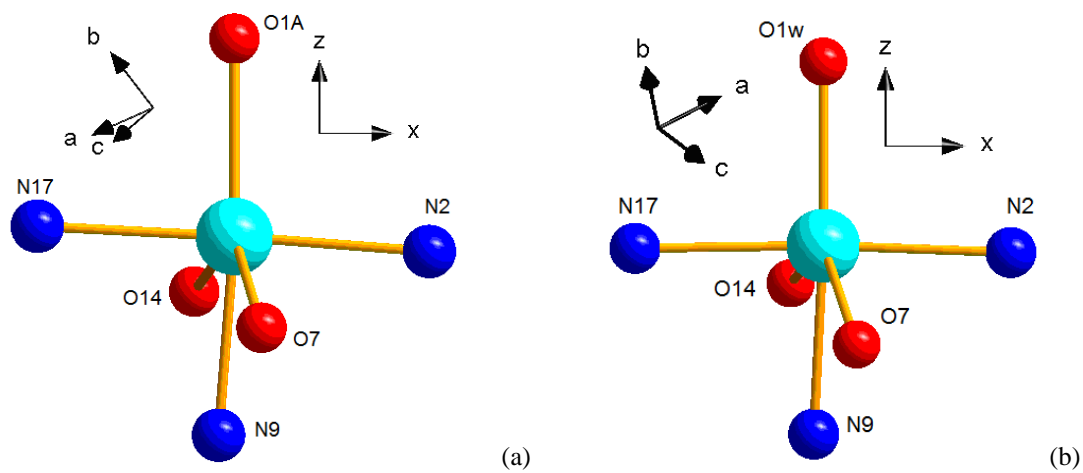


**Figure S26.** Coordination of the nearest ligands around Cu(II) ion in: (a) the complex **1** and (b) **2**. The adopted Cartesian molecular axis system (CMAS) (X, Y, Z) reveals the approximate  $C_2$  symmetry of Cu(II) center.

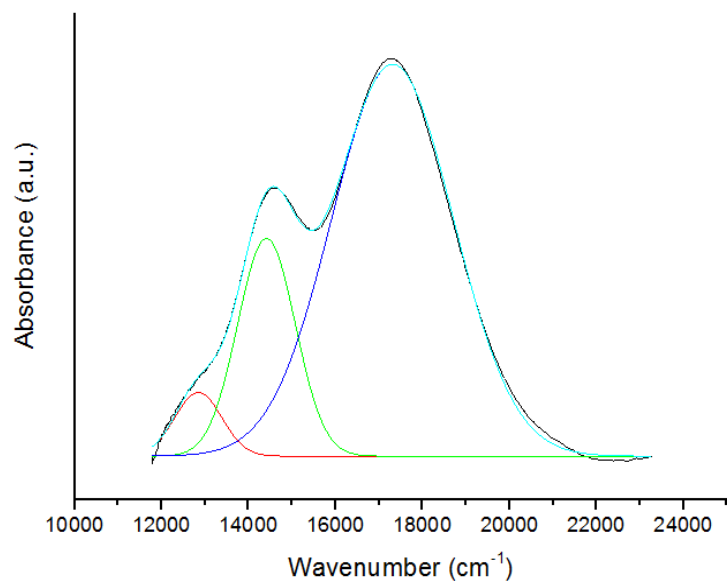


**Figure S27.** Deconvolution of the spectrum of **1** into 3 bands.

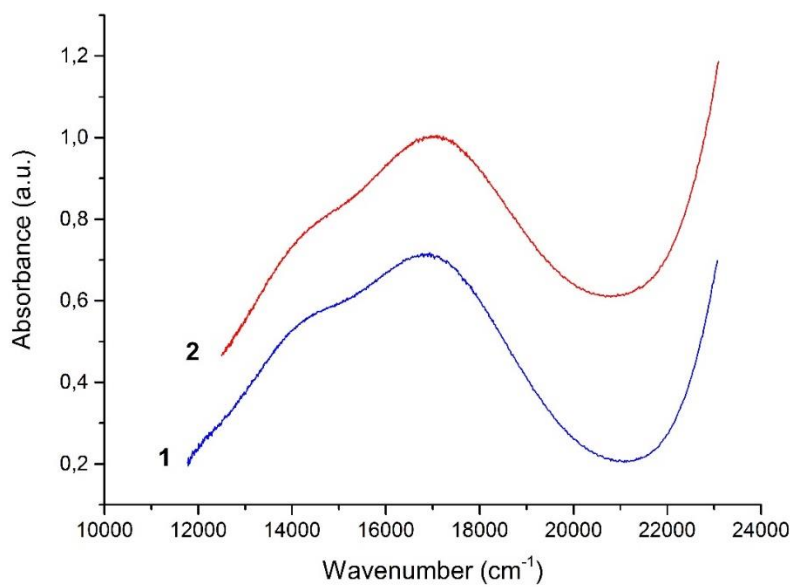


**Figure S28.** Absorption spectrum for the thin film of **1** and **2** measured at RT.

## V. Definitions of the axis systems (ASs) and input sets used for computational modelling of complex **1** and **2**

Note that the crystallographic axis system (CAS) defined in cif file as (a, b, c) for **1** and **2** is non-Cartesian since the space group is P1 for both structures. Hence, we have adopted the Cartesian molecular axis system (X, Y, Z) defined below with respect to the structure of the ML<sub>n</sub> complex in each molecule. So defined AS is equivalent in nature to the notion of the modified crystallographic axis system (CAS\*), irrespective of various ways in which a CAS\* may, in general, be selected for ions in crystals. The nearest surrounding of Cu(II) ion in **1** is formed by three N atoms and three O atoms and the actual site symmetry of Cu(II) center is C<sub>1</sub>. Considering very low symmetry of this ML<sub>n</sub> complex, it is convenient to employ the ascent/descent in symmetry method, for references see, e.g. <sup>41-43</sup>. Here we have selected an axis system, which allows to approximate most closely the actual triclinic symmetry with monoclinic C<sub>2</sub> symmetry. Hence, the axis system (X, Y, Z) was selected with the origin (0, 0, 0) on the Cu atom, the oxygen atom O1A on the z axis, the N2 and N17 atoms almost exactly on the x axis. This Cartesian molecular axis system, denoted for short as CMAS, is defined by the atomic positions ( $\phi$ ,  $\theta$ , R) within the ML<sub>n</sub> complex listed in Table S9 and is depicted in Figure S26.

**Table S9.** The atomic positions ( $\phi$ ,  $\theta$ , R) within the ML<sub>n</sub> complex expressed in the CMAS (X, Y, Z) defined in Figure S26 for sets C<sub>1</sub> and C<sub>2v</sub>.

<b>1</b>				<b>2</b>			
Set C <sub>1</sub>				Set C <sub>1</sub>			
Cu	0.00	0.00	0.000	Cu	0.00	0.00	0.000
N2	-1.09	94.40	1.964	N2	-2.11	92.11	1.985
N17	-178.91	87.01	1.983	N17	-177.89	90.83	1.992
O7	-83.18	111.78	2.472	O7	-80.84	115.25	2.447
O14	100.01	103.42	2.385	O14	98.45	99.65	2.378
N9	146.95	174.57	2.007	N9	111.80	172.26	2.011
O1A	0.00	0.00	1.990	O1w	0.00	0.00	1.943
Set C <sub>2v</sub>				Set C <sub>2v</sub>			
Cu1	0.00	0.00	0.000	Cu	0.00	0.00	0.000
N2	0.00	90.00	1.968	N2	0.00	90.00	1.988
N17	180.00	90.00	1.968	N17	180.00	90.00	1.988
O7	-90.00	107.95	2.439	O7	-90.00	107.45	2.413
O14	90.00	107.95	2.439	O14	90.00	107.45	2.413
N9	90.00	180.00	1.997	N9	90.00	180.00	2.011
O1A	0.00	0.00	1.952	O1w	0.00	0.00	1.943

The CMAS is used in all model calculations to ensure that the results are expressed in compatible axis systems. For the reasons given below, two sets of the atomic positions are considered in this paper as input for modelling.

\* Set denoted as XRD was obtained from the atomic positions (x, y, z) determined by Single Crystal X-Ray diffraction (see Section 2.2) after proper rotation of the whole molecule to express the original (x, y, z) in the CMAS. This set exhibits the actual triclinic C<sub>1</sub> symmetry.

\* Sets denoted as C<sub>2v</sub> and O<sub>h</sub> correspond to orthorhombic C<sub>2v</sub> and cubic O<sub>h</sub> symmetry, respectively. The higher symmetry approximations are considered in the spirit of the ascent/descent in symmetry method<sup>41-43</sup> to facilitate direct comparison with experimental data. These sets were generated by applying symmetrization procedure for the set XRD limited to the ML<sub>n</sub> complex using the module SYMMOL<sup>61, 62</sup> implemented in the WinGX - Version 2018.3 package<sup>63</sup>. The atomic positions ( $\phi$ ,  $\theta$ , R) within the ML<sub>n</sub> complex obtained for the symmetry approximated set C<sub>2v</sub> serve as input only for semiempirical modelling. The cubic O<sub>h</sub> symmetry approximation is employed only for comparison of the CF energy levels and to verify trends observed in CFPs for the respective symmetry cases.

On the one hand, the molecules **1** and **2** exhibit a high degree of structural similarity (see Section 2.2). Their approximate closeness, at the level of the atomic positions ( $\phi$ ,  $\theta$ , R) within the ML<sub>n</sub> complex, may be verified by comparing the respective sets, see Table S9. On the other hand, distinct magnetic behavior of **1** and **2** have been observed, which may possibly be accounted for by the computationally modelled quantities, including the CFP sets and the CF energy levels, the Zeeman factors  $g_i$  and the hyperfine tensor components  $A_i$ . Hence, it is worthwhile to explore the effect of crystallographic structure of **1** and **2** on the modelled quantities at the level of: (a) the actual C<sub>1</sub> symmetry using ab initio modelling (see Section 2.9)

as well as, for comparison, (b) the approximated  $C_{2v}$  symmetry using semiempirical modelling (see Section 2.10). Combination of the two modelling approaches enables comprehensive analysis of the properties of molecules **1** and **2** and correlation of more accurate, but sophisticated, ab initio results (see Section 2.9) with intuitive interpretation of semiempirical results. Semiempirical modelling provides also a simple method for interpreting optical spectra (see Section 2.8). Carrying calculations for two symmetry cases:  $C_1$  and  $C_{2v}$ , enables to study variation of, e.g. the excited state energies and CFPs dominant in each case with the ascent/descent in symmetry as well as the low symmetry aspects inherent in CFP sets. Detailed consideration of these aspects is envisaged in a forthcoming paper.

## VI. Computations using *ab initio* methods

Calculation of hyperfine structure for heavier elements like transition metals is still very demanding in terms of methodology and computer resources.<sup>64</sup> Therefore, we include only preliminary results. Generally, one could calculate reasonable values of the *A* tensor computing 3 terms: Fermi contact term, spin dipolar term and term with contribution of SOC to *A*.<sup>65, 66</sup> Since the *A* tensor depends on distribution of spin density, we have used Gaussian finite nucleus model instead of point-charge model (implemented only for DKH).

In Tables S10 and S11 we calculate the Mulliken populations to show localization of charge and spin of Cu 3*d* electrons and support modelling of compounds with pseudospin Hamiltonian. Table S10 in SI lists Mulliken populations for Cu atom and neighboring N and O atoms based on X-ray structures of complexes **1** and **2**. The results show localization of charge and spin of Cu 3*d* electrons and support modelling of compounds with pseudospin Hamiltonian<sup>22</sup> with value of spin equal to  $S = \frac{1}{2}$  (Sections IV and V in SI). Results of Mulliken analysis show that on 3*d* orbitals there are 9.295 electrons, close to nominal value of 9. Spin for 3*d* shell is equal to 0.691, leaking mainly to N atoms. Expectation value of operator of total  $S^2$  is equal to 0.7521, close to ideal value of 0.75. Neighboring O atoms are more electrically polarized than nitrogen atoms suggesting more ionic bonds, which is also supported by Loewdin and Mayer analysis<sup>8</sup> (Table S11). The N atoms are more spin polarized than O atoms, suggesting that Cu-N are more covalent bonds.

Energies of standard B3LYP hybrid functional are underestimated with respect to the CAM-B3LYP results. For functional CAM-B3LYP three methods were utilized: (i) (simplified) Tamm-Dancoff Approximation<sup>14</sup>, (ii) (simplified) TDDFT<sup>15</sup> and (iii) full TDA.<sup>67</sup> Mulliken populations are listed in Table S12 and for the ground state these values are similar to those calculated using standard DFT, whereas energies of excited states are listed in Table S13. Local charges and spins are almost identical for methods (i) and (ii), but energies of sTDA and TDA (Table S13) are closer to those calculated using multiconfigurational SCF methods. Since molecules possess the  $C_1$  symmetry, the Kohn-Sham orbitals (microstates) in the ground state may be degenerated only due to accidental degeneracy of spin orbitals. One-electron occupancies of microstates contributing to the ground state were therefore studied and B3LYP results show (due to finite electronic smearing) approximate order of KS orbitals.

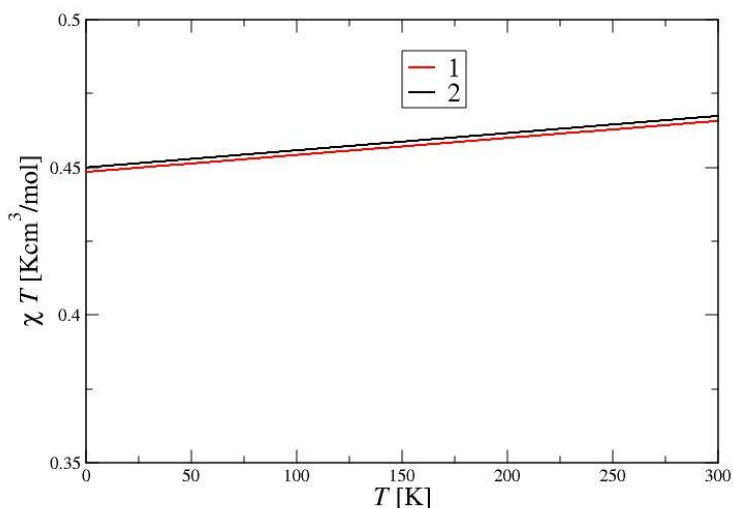
These computations yield an approximate order of KS orbitals with major contribution of atomic 3*d* orbital as: the lowest energy microstate is the doubly occupied 3*dxz* and ( $\alpha$  spin orbital) 3*dz*<sup>2</sup> with minor admixture of 3*dx*<sup>2</sup>-*y*<sup>2</sup>, followed by 3*dyz* and 3*dxy* orbitals. Next is well separated in energy 3*dx*<sup>2</sup>-*y*<sup>2</sup>, which is the closest occupied orbital to the Fermi level. First unoccupied orbital is 3*dz*<sup>2</sup> with minor admixture of 3*dx*<sup>2</sup>-*y*<sup>2</sup> ( $\beta$  spin orbital). Occupied ( $\alpha$  spin orbital) counterpart of this spinorbital is the 3*dz*<sup>2</sup> lying near 3*dxz* microstate. Electron occupying this orbital gives main contribution to the magnetic moment. Grouping of electrons is similar to that for higher symmetry cubic case for 3*d*<sup>*p*</sup> ions, namely the degenerated state  $t_{2g}$  (3*dxy*, 3*dyz*, 3*dxz*) is separated from the degenerated state  $e_g$  (3*dx*<sup>2</sup>-*y*<sup>2</sup>, 3*dz*<sup>2</sup>) lying closer to the Fermi level. The real 3*d* orbitals are expressed in the Cartesian molecular axis system (CMAS) defined in Section V in SI. All 4 excited states within the ground multiplet <sup>2</sup>D of Cu(II; 3*d*<sup>*p*</sup>) ion originate from excitations of electron density from occupied orbitals to only one  $\beta$  unoccupied orbital closest to Fermi level (number 167b in ORCA output). This microstate has mainly 3*dz*<sup>2</sup> character consistent with DFT results where unpaired electron (lone hole) in the ground state is of such symmetry. First excited state results mainly from excitation of 3*dx*<sup>2</sup>-*y*<sup>2</sup> electron to 167b state, so we could approximate such state with hole on 3*dx*<sup>2</sup>-*y*<sup>2</sup> orbital. Second and third excited states result from excitation of electron from *dxy* and 3*dyz* orbitals, fourth from 3*dxz*, 3*dyz* and 3*dxy* orbitals. Since TDDFT excited states are due to the *d*-electron excitations similarly as in the crystal field picture, we assume that such TDDFT states correspond to the CF states.

In Table S13 excited states were calculated for complex **1**, in Table S14 Mulliken, Loewdin and Mayer populations were calculated using CASSCF approach, while Table S16 presents compositions of wavefunctions for one chosen state from each Kramers doublet for complexes **1** and **2**. In Table S17 we list values of the *A* tensor obtained using CASSCF and DFT. MC-SCF methods are problematic for obtaining hyperfine constants due to difficulties with determining correct spin densities in areas close to nuclei.<sup>68</sup> Therefore we rely mainly on DFT methods<sup>64</sup>, where we have used increased accuracy and combined the basis aug-cc-pVTZ-J and CP(PPP) for Cu atom. The closest results to experimental ones are obtained in the 0th order of DKH correction to *A*, but the results seem not reliable since 2nd order DKH correction to *A* and DFT ZORA are smaller by up to two orders of magnitude.

The inclusion of NEVPT2 dynamic corrections for complex **1** shifts the 1<sup>st</sup> excited state  $\sim 3000$  cm<sup>-1</sup> up from the ground state, and  $\sim 4000$  cm<sup>-1</sup> for the 2<sup>nd</sup>, 3<sup>rd</sup> and 4<sup>th</sup> excited states. Difference between the 1<sup>st</sup> excited state and 2<sup>nd</sup> excited state is enlarged from  $\sim 700$  cm<sup>-1</sup> to  $\sim 1600$  cm<sup>-1</sup>. Differences between the higher excited states obtained by

CASSCF and NEVPT2 are similar. This suggests that dynamical correlations are most relevant for the two lowest states with the unpaired  $3dx^2-y^2$  and  $3dz^2$  electrons contributing to the magnetic moment. Because accurate description of electronic correlations is crucial for optical spectra, the *ab initio* results are next mapped on effective models to allow comparison with CF energy levels and semiempirical results in Sections 2.8 and 2.10 respectively.

Consequences of the enlarged separations of states due to inclusion of dynamic correlations at NEVPT2 level are as follows. Due to such large separations, the mixing of states by SOC is small. The Kramers doublet states resulting from action of SOC (Table S15) indicate that the relative energies are slightly changed with exception of 3<sup>rd</sup> and 4<sup>th</sup> excited states, which are now clearly separated in energy, while each being a Kramers doublet, as expected for  $S = 1/2$ . We have listed compositions of wavefunctions for one chosen state from each Kramers doublet for complexes **1** and **2** in Table S16. Such states consist of two components:  $|S, +M_S\rangle$  and  $|S, -M_S\rangle$  with respective mixing coefficients. Second states from each Kramers doublet have mixing coefficients interchanged for the components  $|S, +M_S\rangle$  and  $|S, -M_S\rangle$ . In the case of complex **1** three lowest KD states consist mainly of one chosen spin free state (i.e. root) with arbitrary spin direction with minor addition of the second spin free state with spin of opposite direction. The fourth and fifth KD states are mixtures of spin free states originating from two roots, which are the 3<sup>rd</sup> and 4<sup>th</sup> excited NEVPT2 states. This is not surprising since the latter ones are relatively closer in energy and SOC mixes them stronger. For complex **2**, since all NEVPT2 spin free states are well separated, KD states are only mixtures of states originating from one root.



ap

**Figure S29.**  $\chi T$  plots versus temperature calculated with NEVPT2 for both compounds.

**Table S10.** Results of Mulliken populations for selected atoms (denoted by cif symbols) calculated using B3LYP DFT and CASSCF for complexes **1** and **2**. Charges are in units of  $|e|$  and spin in Bohr magnetons.

<b>1</b>	B3LYP		CASSCF		B3LYP		CASSCF		<b>2</b>	
	Atom	Charge	Spin	Charge	Spin	Charge	Spin	Charge		Spin
	Cu1	0.6856	0.6688	1.2939	0.9788	0.3863	-0.014	1.1559	0.9724	Cu1
	O7	-0.4239	-0.0002	-0.6731	0.0009	-0.3923	0.0006	-0.6536	0.0008	O7
	N9	-0.1682	0.1273	-0.572	0.0045	-0.2259	0.3141	-0.7979	0.0037	N9
	O14	-0.4232	0.0001	-0.6628	0.0007	-0.3989	0.0017	-0.6483	0.0008	O14
	N2	-0.1406	0.0798	-0.3651	0.0039	-0.1358	0.04	-0.3350	0.0035	N2
	N17	-0.1746	0.0762	-0.4903	0.0041	-0.1244	0.0307	-0.3598	0.0038	N17
	O1A	-0.3631	0.0347	-0.5597	0.0024	-0.1829	0	-0.3085	0.0025	O1W

**Table S11.** Mulliken populations for selected atoms calculated using B3LYP for complex **1** and basis set ZORA-def2-SVP with exception of (\*), where basis is def2-SPV. Charges are in units of |e| and spin in Bohr magnetons; notation of atoms (symbol and number) is as in cif file.

Atom:	*Mulliken		Mulliken		Loewdin		Mayer
	Charge	Spin	Charge	Spin	Charge	Spin	Charge
Cu1	0.5682	0.641	0.6856	0.6688	0.3097	0.6823	0.6856
O7	-0.4248	-0.0002	-0.4239	-0.0002	-0.1395	-0.0008	-0.4239
N9	-0.1236	0.1381	-0.1682	0.1273	0.0182	0.1132	-0.1682
O14	-0.4243	0.0001	-0.4232	0.0001	-0.114	-0.0004	-0.4232
N2	-0.1011	0.0857	-0.1406	0.0798	-0.0142	0.0721	-0.1406
N17	-0.133	0.0821	-0.1746	0.0762	-0.0285	0.0684	-0.1746
O1A	-0.2874	0.0351	-0.3631	0.0347	0.0361	0.0383	-0.3631

**Table S12.** Mulliken populations for selected atoms calculated using CAM-B3LYP for complex **1**; charge is in units of |e| and spin is in Bohr magnetons.

Atom:	sTDA		sTDDFT	
	charge	spin	charge	spin
Cu1	0.6929	0.6986	0.6929	0.698
O7	-0.4182	-0.0004	-0.4182	-0.0004
N9	-0.1573	0.1175	-0.1574	0.1187
O14	-0.4166	-0.0002	-0.4165	-0.0002
N2	-0.1373	0.0755	-0.1373	0.0757
N17	-0.1714	0.0717	-0.1715	0.0719
O1A	-0.3647	0.0338	-0.3646	0.0339

**Table S13.** Energies of the excited states w.r.t. the ground state (in  $\text{cm}^{-1}$ ) calculated using CAM-B3LYP for complex **1**; results for B3LYP are shown for comparison.

Excited state	CAM-B3LYP sTDA	CAM-B3LYP sTDDFT	CAM-B3LYP TDA	B3LYP
1st	12547	19471	12574	1360
2nd	17767	19706	17761	2920
3rd	17880	21108	17907	3517
4th	18512	21839	18578	4015

**Table S14.** Mulliken, Loewdin and Mayer populations for selected atoms of complexes **1** and **2** calculated using CASSCF approach. Basis sets is of ZORA-def2-SVP with exception of \*where basis is def2-SPV. Charges are in units of |e| and spin in Bohr magnetons; notation of atoms (symbol and number) is as in cif file.

<b>1</b>	Mulliken <b>1</b>		Loewdin <b>1</b>		Mayer <b>1</b>	Mulliken <b>2</b>		<b>2</b>
	Charge	Spin	Charge	Spin	Charge	Charge	Spin	
Atom	Charge	Spin	Charge	Spin	Charge	Charge	Spin	Atom
Cu1	1.2939	0.9788	0.6336	0.9727	1.2939	1.1559	0.9724	Cu01
O7	-0.6731	0.0009	-0.2295	0.0016	-0.6731	-0.6536	0.0008	O7
N9	-0.572	0.0045	-0.0884	0.0052	-0.572	-0.6483	0.0008	O14

O14	-0.6628	0.0007	-0.2331	0.0013	-0.6628	-0.3085	0.0025	O1W
N2	-0.3651	0.0039	-0.0961	0.0045	-0.3651	-0.3350	0.0035	N2
N17	-0.4903	0.0041	-0.117	0.0045	-0.4903	-0.7979	0.0037	N9
O1A	-0.5597	0.0024	-0.0422	0.0038	-0.5597	-0.3598	0.0038	N17

**Table S15.** Energies of Kramers doublet (KD) states (in  $\text{cm}^{-1}$ ) for complexes **1** and **2**.

KD number	CASSCF <b>1</b>	NEVPT2 <b>1</b>	CASSCF <b>2</b>	NEVPT2 <b>2</b>
0 (GS)	0	0	0	0
1	9486	12515	9821	12196
2	10355	14170	10436	13959
3	12157	16071	12332	16566
4	13013	16893	13690	18353

**Table S16.** Composition of spin-orbit relativistic states being linear combinations of the nonrelativistic NEVPT2 states mixed by SOC, which are denoted as: |number of root, S,  $M_S$ >. Only states with major weights are listed. Number of root means the consecutive number of NEVPT2 state (0 is ground state (GS), 1 is 1<sup>st</sup> excited state etc.).

KD number	KD states for complex <b>1</b>	KD states for complex <b>2</b>
0 (GS)	0.7682 0 1/2 -1/2>+0.2278 0 1/2 +1/2>	0.8788 0 1/2 -1/2>+0.1168 0 1/2 +1/2>
1	0.836 1 -1/2 -1/2>+0.11 1 1/2 +1/2>	0.7245 1 -1/2 -1/2>+0.24 1 1/2 +1/2>
2	0.702 2 1/2 +1/2>+0.19 2 1/2 -1/2>	0.87 2 1/2 +1/2>+0.07 2 1/2 -1/2>
3	0.373 4 1/2 +1/2>+0.272 3 1/2 -1/2>+0.207 3 1/2 +1/2>	0.48 3 1/2 +1/2>+0.42 3 1/2 -1/2>
4	0.487 4 1/2 -1/2>+0.387 3 1/2 -1/2>	0.9 4 1/2 +1/2>

**Table S17.** The A-tensor components (in  $10^{-4} \text{cm}^{-1}$ ) for complex **1** obtained using ZORA approach and DKH one (including SOC correction of the 0<sup>th</sup> or 2<sup>nd</sup> order).

A-tensor	CASSCF DKH (2 <sup>nd</sup> )	B3LYP DKH (0 <sup>th</sup> )	B3LYP DKH (2 <sup>nd</sup> )	B3LYP ZORA
$A_x$	-0.394	13.982	-0.4	-0.398
$A_y$	-0.4	63.085	-0.459	-0.4
$A_z$	0.837	65.225	0.853	0.853

We have calculated the A-tensor components ( $A_x$ ,  $A_y$ ,  $A_z$ ) in the principal axis system (PAS) using CASSCF and DFT approach. Results are provided in Section V in SI. The free (spherical symmetry) Cu(II;  $3d^9$ ) ion has only one (ground) multiplet  $^2D$ , which splits in octahedral symmetry CF into the lowest orbital doublet  $^2E_g$  and higher orbital triplet  $^2T_{2g}$ .<sup>29</sup> We associate tentatively the ground state and the 1st excited state in Table 3 as originating from the doublet, whereas the other excited states from the triplet. This sequence depends on the CF strength and the  $^2E_g$ - and  $^2T_{2g}$ -states may also intertwine. It is also validated by B3LYP one-electron occupancies of microstates (Kohn-Sham orbitals) contributing to the ground state. To estimate roughly the value of the cubic CFP  $Dq$ , we averaged energies of NEVPT2 states contributing to  $^2E_g$  and  $^2T_{2g}$ . Their difference yields approximate value of the cubic CF splitting  $10Dq$  as  $9213 \text{cm}^{-1}$ , so  $Dq \sim 921.3 \text{cm}^{-1}$ , close to literature data<sup>29</sup> of  $1210 \text{cm}^{-1}$ . The estimation of  $Dq$  from TDA TDDFT yields  $Dq$  as  $1179.5 \text{cm}^{-1}$ , which is closer to literature data and compares well with those determined in Section 2.8.

We have computed *ab initio* Ligand Field (LF) parameters, i.e. the matrix elements of  $V_{LF}$  and Racah parameters (A, B, C) as implemented in ORCA.<sup>23, 24</sup> For the chosen active space in CASSCF or NEVPT2 a unitary operation

is done to set all roots closest to  $L_z$  single-configurational solutions. In single-electron picture these 5 states correspond to the real  $3d$  orbitals (or their combinations). Ligand field is understood as effective field acting on single particle. Corresponding orbital energies obtained using CASSCF and NEVPT2 are listed in Table S18. As expected for  $d^1$  or  $d^9$  ions the computed Racah parameters B and C, which involve two-electron integrals, are zero, whereas  $A = 217937 \text{ cm}^{-1}$  and  $A = 215623 \text{ cm}^{-1}$  for complex **1** and **2**, respectively. Analysis of the LF results of NEVPT2 for complex **1** indicates what follows. The energy  $16215 \text{ cm}^{-1}$  of state with main contribution of  $3dz^2$  electron is taken as reference energy. Then absolute energy differences between this energy and the excited states energies are:  $12680 (3dx^2-y^2)$ ,  $14255 (3dxz)$ ,  $16186 (3dxy)$ , and  $16215 (3dyz)$ . These energy differences are almost identical to NEVPT2 energies. This approach yields the lowest state as  $3dz^2$  hole, next state as  $3dx^2-y^2$ , next two states as mixed  $3dxz$  and  $3dyz$ , and the highest state as  $3dxy$ . This assignment of the single-electron orbitals should correspond directly to semiempirical results obtained using SPM/CFP for set  $C_{2v}$  upon diagonalization of CF Hamiltonian within the  $|L=2, M_L\rangle$  states of  $^2D$  multiplet (Section 2.10). One-electron excitations from the ground state  $3dz^2$  to the 1st excited state  $3dx^2-y^2$  correspond to optical transitions between NEVPT2 molecular states, so our MC-SCF spectrum could be well modeled using LF model with single-particle states expressed as  $3d$  real orbitals. There is also agreement with TDDFT results, where excitations are mainly due to hopping of  $3d$  electrons to the first unoccupied orbital. Additionally, to gain better insight into optical spectroscopy results (Section 2.8), using pure dipole approximation within NEVPT2 and CASSCF, we have calculated wavelengths corresponding to optical transitions of CD and UV spectra. These values are (in nm): (788.6, 701.5, 617.8, 616.7) and (1031, 959.5, 818.8, 815.5), after conversion to  $[\text{cm}^{-1}]$  yield (12680, 14255, 16186, 16215) and (9699, 10420, 12212, 12262), respectively, which in the first case compare very well with the experimental energy values of the transitions (12743, 14441, 17073, 18056) (Section 2.8).

**Table S18.** Orbital energies (in  $\text{cm}^{-1}$ ) calculated using ab initio Ligand Field for complexes **1** and **2**. Orbitals expressed as the real  $3d$  functions correspond to respective LF states.

<b>1</b> $3d$ -orbitals:	$z^2$	$x^2-y^2$	$xz$	$xy$	$yz$
CASSCF	12263	2564	1841	50	0
NEVPT2	16215	3535	1960	29	0
<b>2</b> $3d$ -orbitals:	$z^2$	$x^2-y^2 + xz$	$x^2-y^2 + xz$	$yz$	$xy$
CASSCF	13228	3256	2681	1095	0
NEVPT2	18030	5749	3982	1609	0

## VII. SPM and MSH analysis

The simplified MSH formulas<sup>29, 59</sup> for the factors  $g_i$  were derived for Cu(II;  $d^9$ ,  $S = 1/2$ ) in a tetragonally distorted octahedron. In regular situations, when the EPR spectra are axial with equivalent x and y axes and two  $g$  values,  $g_{\parallel}$  ( $g_z$ ) and  $g_{\perp}$  ( $g_x = g_y$ ), the ground state may be the  $|dx^2-y^2\rangle$  or  $|dz^2\rangle$ . The following formulas were derived assuming the ground state as  $dx^2-y^2$ , which applies to elongated octahedral, square pyramidal or square planar geometry:<sup>29, 59</sup>

$$g_{\parallel} = 2.0023 \pm \frac{8\xi}{E(d_{x^2-y^2}) - E(d_{xy})} \quad (S6)$$

$$g_{\perp} = 2.0023 \pm \frac{2\xi}{E(d_{x^2-y^2}) - E(d_{xz})} = 2.0023 \pm \frac{2\xi}{E(d_{x^2-y^2}) - E(d_{yz})} \quad (S7)$$

For Cu(II;  $d^9$ ,  $S = 1/2$ ) complexes the + sign applies in Eqs S6 and S7, so the  $g_i$  factors are higher than  $g_e (= 2.0023)$ . Eqs S6 and S7 include only the spin-orbit coupling ( $\zeta$ ) contributions arising from the second order perturbation theory, which may be not adequate for more realistic predictions. Similar formulas apply for the ground state  $|dz^2\rangle$ , which is an alternative option for the idealized tetragonal site symmetry of a compressed octahedron.

A few important points bearing on reliability of usage of SPM/CFP predictions as input data for MSH formulas must be considered.

(a) The CFPs obtained for set  $C_{2v}$  (see Table 5) turn out to be highly non-standard<sup>24, 25</sup>, since the respective rhombicity ratios,  $B_{22} / B_{20}$ , are much greater than the maximum rhombicity ratio, i.e. 0.408, for CFPs in Wybourne notation. Hence, for the reason given in point (b), orthorhombic standardization (OR/ST)<sup>69, 70</sup> was carried out. In general, the process of standardization limits the rhombicity ratio for CFPs in the Wybourne notation to the range (0, 0.408), whereas CFPs or ZFSPs in the ESO notation to the range (0, 1) by a proper choice of the axis system. Pertinent calculations are facilitated by the computer package CST.<sup>71, 72</sup> Note that applications of the standardization amply indicate the advantage of systematic data presentation the parameter sets expressed in a unique standardized form that ensures compatibility of data taken from various sources, see, e.g. for CFP sets<sup>69, 70, 73-76</sup>, whereas for ZFSP sets<sup>69, 77-79</sup>, and references therein. The standardized CFP sets are denoted in Table 4 as set  $C_{2v}$  after OR/ST.

(b) In the case of employing the CFPs obtained for set  $C_{2v}$  and set  $C_{2v}$  after OR/ST as input for a diagonalization program within the full  $3d^9$  configuration, the same energy levels would be obtained, since the standardization transformations leave  $H_{CF}$  rotationally invariant.<sup>24-31</sup> However, when employing the approximated MSH formulas<sup>34-40, 80-82</sup> this may not be the case for two reasons. First, the energies  $E_i$  in Eq. (3) and (4) below are not exact solutions. Several approximations were made during derivations of the MSH formulas using the higher order perturbation theory. Hence, it is essential to ensure that the CFP sets to be used as input for subsequent MSH modelling exhibit the highest values of the dominant CFPs, i.e. those corresponding to higher symmetry, while the minimal values of the CFPs corresponding to lower symmetry. In this case, we shall maximize the tetragonal CFPs:  $B_{20}$ ,  $B_{40}$  and  $B_{44}$ , while minimizing the remaining orthorhombic CFPs. These conditions are ensured by application of proper orthorhombic standardization, which yields standardized CFP sets.

The points that bear on interpretation of results in Table S19 are as follows. (i) The numbering ( $i = 1 - 4$ ) of CF energies ( $E_i$ ) does not reflect any ordering in magnitude. In Eq. (2),  $E_4$  represents the splitting of the lower orbital E-doublet. The values of  $E_4$  are obtained as negative in our calculations. However, for proper interpretation of the sequence of CF energies (-) sign of  $E_4$  must be changed to (+) sign, since here it only reflects the change of the nominal ground state within the lower orbital E-doublet from one option to another, i.e. either  $|dx^2-y^2\rangle$  or  $|dz^2\rangle$ . So the negative  $E_4$  sign affects only that the sequence of the states assigned to the first two CF energy levels and indicates that they should be inverted:  $|dx^2-y^2\rangle \leftarrow \rightarrow |dz^2\rangle$ . It does not mean that the negative value of  $E_4$  should be taken as the ground level and other levels rescaled to such ground level set to zero. This finding bears significantly on interpretation of CF energies obtained from Eq. (2) and proper comparison with optical spectra presented in Section 2.8. Note that for monoclinic  $C_2$  and triclinic  $C_1$  symmetry the ground state becomes an admixture of both states  $|dx^2-y^2\rangle$  and  $|dz^2\rangle$  (Sections 2.8 and 2.9). (ii) It should also be noted that by reducing the set of four orthorhombic CF energies  $E_i$  ( $i = 1 - 4$ ) in Eq. (2) to the tetragonal case by setting orthorhombic CFPs to zero, instead of two CF energies  $E_i$  ( $i = 1, 2$ ) in Eq. (1), we obtain three CF energies:  $E_1$ ,  $E_2 = E_3$  and  $E_4$ . This mismatch arises from omission in<sup>35, 38, 83</sup> of the third CF energy level  $E_4$ , which exists for tetragonal symmetry. This can be checked by reducing orthorhombic equations for  $g_i$  and  $A_i$  to tetragonal case. Then, it turns out that the CF energy  $E_4$ , which represents the splitting of the lower orbital E-doublet for tetragonal symmetry, gives no contributions to  $g_i$  and  $A_i$ . It appears

that for this reason  $E_4$  was simply omitted in MSH formulas in source papers.<sup>34-40</sup> (iii) There is an apparent problem: how to explain that the  $Dq$  values in the lower (OR) part of Table 9 differ from those in the upper (TE) part, which are equal to the respective ‘input’  $Dq$  values? This is due to different formulas adopted in calculations of the cubic CF parameter  $Dq$  in the TE and OR case. The  $Dq$  values adopted in the TE case are those experimentally determined from optical spectra, which directly correspond to  $E_1$  in Eq. (1), whereas no specific relation was provided for  $Dq$  in.<sup>34-40</sup> However, in the OR case  $Dq$ , i.e.  $E_1$  in Eq. (2), is calculated using the relation:<sup>80-82</sup>  $Dq = \sqrt{70/105} B_{44}$ . The differences between the OR and TE  $Dq$  values amount up to about 30% for set  $C_{2v}$  after OR/ST, whereas only 5% for set  $C_{2v}$ .

**Table S19.** The conventional CFPs calculated using the CFPs  $B_{kq}$  in Table 5 together with energy levels:  $E_i$  (all in  $\text{cm}^{-1}$ ) and SHPs:  $g_i$  (dimensionless) and  $A_i$  (in  $10^{-4} \text{ cm}^{-1}$ ).

	TE formulas adopted							
	Complex 1				Complex 2			
	$C_{2v}$		$C_{2v}$ after OR/ST		$C_{2v}$		$C_{2v}$ after OR/ST	
$Dq$	1285	1015	1285	1015	1285	1015	1285	1015
$Ds$	-2276	-1798	4103	3241	-2288	-1807	3819	3017
$Dt$	-282	-222	873	689	-293	-232	818	646
$E_1$	12850	10150	12850	10150	12850	10150	12850	10150
$E_2$	7431	5869	20794	16427	7452	5886	20218	15972
$g_x$	2.1168	2.1469	2.0499	2.0646	2.1165	2.1464	2.0510	2.0659
$g_y$	2.2879	2.3699	2.2713	2.3432	2.2879	2.3697	2.2715	2.3435
$A_x$	16.1	22.9	0.9	4.2	16.0	22.8	1.1	4.5
$A_y$	-171.9	-152.0	-168.4	-149.5	-171.9	-152.0	-168.5	-149.6
	OR formulas adopted							
$Dq$	1220	963	1893	1495	1181	932	1829	1444
$Ds$	-2276	-1798	4103	3241	-2288	-1807	3819	3017
$Dt$	-282	-222	873	689	-293	-232	818	646
$D\zeta$	1977	1561	-150	-118	1783	1409	-252	-199
$D\eta$	610	482	129	102	559	442	96	76
$E_1$	12195	9627	18931	14945	11810	9324	18293	14441
$E_2$	3287	2589	27839	21983	3300	2599	26804	21165
$E_3$	10266	8104	25910	20460	9526	7520	24519	19361
$E_4$	10512	8303	20775	16409	10619	8387	19367	15296
$g_x$	2.2423	2.3003	2.0358	2.0455	2.2420	2.2997	2.0371	2.0473
$g_y$	2.1008	2.1342	2.0382	2.0487	2.1063	2.1406	2.0403	2.0514
$(g_x+g_y)/2$	2.1716	2.2173	2.0370	2.0471	2.1742	2.2202	2.0387	2.0494
$g_z$	2.3236	2.4232	2.1852	2.2341	2.3343	2.4372	2.1916	2.2425
$A_x$	140.1	154.7	84.2	86.4	139.6	154.2	84.5	86.8
$A_y$	-83.0	-76.9	-88.3	-85.9	-81.4	-75.0	-87.8	-85.2
$(A_x+A_y)/2$	28.55	38.9	-2.05	0.25	29.1	39.6	-1.65	0.8
$A_z$	-126.4	-92.0	-183.1	-167.7	-123.0	-87.6	-181.1	-165.0

**Table S20.** The axial  $g_i$  (dimensionless) and hyperfine parameters  $A_i$  (in  $10^{-4} \text{ cm}^{-1}$ ) reported for Cu(II) ions in various compounds.

Compound	$g_{\parallel}$	$g_{\perp}$	$A_{\parallel}$	$A_{\perp}$	Ref.	$10Dq$
CaB <sub>4</sub> O <sub>7</sub> : CuO	2.32	2.06	146.4 [154.5]*	27.0 [28.5]	Expt. <sup>84</sup>	
	2.32	2.06	-154	-28	Theo. <sup>35</sup>	13330
LiRbB <sub>4</sub> O <sub>7</sub> : CuO	2.4451	2.0561	158	-	Expt. <sup>85</sup>	
	2.445	2.058	-166	-22	Theo. <sup>36</sup>	
[CuL <sub>2</sub> ] 2MeOH <sup>&amp;</sup>	2.260	2.050	158.2 [167]*#	-	Expt. <sup>86</sup>	

\* The original  $A_i$  values in units of [Gauss] were converted to [ $\text{cm}^{-1}$ ] using relation:  $P [\text{Gauss}] \Rightarrow g \times 0.4669 \times P [10^{-4} \text{ cm}^{-1}]$ , where  $g$  is the spectroscopic splitting factor.

& L – deprotonated form of 2-methoxy-6-(E-2-pyridyliminomethyl)-phenol.

# No units were assigned for the value 167 but since EPR spectra were in [G], we assumed [G] for  $A_i$ .

## VIII. Literature

1. N. T. Coogan, M. A. Chimes, J. Raftery, P. Mocilac and M. A. Denecke, *J. Org. Chem.*, 2015, **80**, 8684-8693.
2. RigakuOxfordDiffraction, *CrysAlisPro 1.171.39.46*, 2018.
3. G. Sheldrick, *Acta Cryst. C*, 2015, **71**, 3-8.
4. S. Stoll, *EasySpin: An EPR Toolbox for Matlab - version 3.0.0 available from the website: <http://www.easyspin.org>*, 2008.
5. S. Stoll and A. Schweiger, *Journal of Magnetic Resonance*, 2006, **178**, 42-55.
6. G. A. Bain and J. F. Berry, *J. Chem. Educ.*, 2008, **85**, 532.
7. W. Haase, *Ber. Bunsenges. Phys. Chem.*, 1994, **98**, 1208-1208.
8. F. Neese, *WIREs Comput. Mol. Sci.*, 2012, **2**, 73-78.
9. M. Atanasov, D. Aravena, E. Suturina, E. Bill, D. Maganas and F. Neese, *Coord. Chem. Rev.*, 2015, **289-290**, 177-214.
10. P. J. Stephens, F. J. Devlin, C. F. Chabalowski and M. J. Frisch, *J. Phys. Chem.*, 1994, **98**, 11623-11627.
11. P.-Å. Malmqvist and B. O. Roos, *Chem. Phys. Lett.*, 1989, **155**, 189-194.
12. Y. Rechkemmer, F. D. Breitgoff, M. van der Meer, M. Atanasov, M. Hakl, M. Orlita, P. Neugebauer, F. Neese, B. Sarkar and J. van Slageren, *Nat. Commun.*, 2016, **7**, 10467.
13. T. Petrenko, S. Kossmann and F. Neese, *J. Chem. Phys.*, 2011, **134**, 054116.
14. S. Grimme, *J. Chem. Phys.*, 2013, **138**, 244104.
15. C. Bannwarth and S. Grimme, *Comput. Theo. Chem.*, 2014, **1040-1041**, 45-53.
16. T. Yanai, D. P. Tew and N. C. Handy, *Chem. Phys. Lett.*, 2004, **393**, 51-57.
17. P. Å. Malmqvist, B. O. Roos and B. Schimmelpfennig, *Chem. Phys. Lett.*, 2002, **357**, 230-240.
18. E. v. Lenthe, E. J. Baerends and J. G. Snijders, *J. Chem. Phys.*, 1993, **99**, 4597-4610.
19. M. Reiher, *WIREs Comput. Mol. Sci.*, 2012, **2**, 139-149.
20. F. Neese, A. Wolf, T. Fleig, M. Reiher and B. A. Hess, *J. Chem. Phys.*, 2005, **122**, 204107.
21. B. Sandhoefer and F. Neese, *J. Chem. Phys.*, 2012, **137**, 094102.
22. D. Ganyushin and F. Neese, *J. Chem. Phys.*, 2006, **125**, 024103.
23. M. Atanasov, D. Ganyushin, K. Sivalingam and F. Neese, in *Molecular Electronic Structures of Transition Metal Complexes II*, eds. D. M. P. Mingos, P. Day and J. P. Dahl, Springer Berlin Heidelberg, Berlin, Heidelberg, 2012, DOI: 10.1007/430\_2011\_57, pp. 149-220.
24. E. A. Suturina, D. Maganas, E. Bill, M. Atanasov and F. Neese, *Inorg. Chem.*, 2015, **54**, 9948-9961.
25. D. J. Newman and B. Ng, *Rep. Prog. Phys.*, 1989, **52**, 699-762.
26. C. Rudowicz, P. Gnutek and M. Açıkgöz, *Appl. Spectrosc. Rev.*, 2019, **54**, 673-718.
27. C. A. Morrison, in *Crystal Fields for Transition-Metal Ions in Laser Host Materials*, ed. C. A. Morrison, Springer Berlin Heidelberg, Berlin, Heidelberg, 1992, DOI: 10.1007/978-3-642-95686-7\_1, pp. 1-2.
28. B. G. Wybourne, *Spectroscopic Properties of Rare Earths*, Interscience Publishers, 1965.
29. A. Abragam and B. Bleaney, *Electron Paramagnetic Resonance of Transition Ion*, Clarendon Press, Oxford, 1970.
30. F. E. Mabbs and D. Collison, *Electron Paramagnetic Resonance of d Transition-Metal Compounds*, Elsevier, Amsterdam 1992.
31. S. K. Misra, Ed. *Multifrequency Electron Paramagnetic Resonance; Erratum S.K. Misra, C. Rudowicz, <http://www.wiley-vch.de/publish/dt/books/ISBN3-527-40779-0/>*. Wiley-VCH, Weinheim 2011.
32. C. Rudowicz, *Magn. Reson. Rev.*, 1987, **13**, 1.
33. C. Rudowicz and M. Karbowski, *Coord. Chem. Rev.*, 2015, **287**, 28-63.
34. Z. Wen-Chen and W. Shao-Yi, *Z. Naturforsch.*, 2000, **55**, 915-917.
35. M.-Q. Kuang, L.-D. Wang and S.-K. Duan, *J. Phys. Chem. Solids*, 2017, **111**, 41-46.
36. H.-M. Zhang and X. Wan, *J. Non-Cryst. Solids*, 2013, **361**, 43-46.
37. S.-Y. Wu, H.-M. Zhang, P. Xu and S.-X. Zhang, *Spectrochim. Acta A*, 2010, **75**, 230-234.
38. M.-Q. Kuang, S.-Y. Wu, G.-L. Li and X.-F. Hu, *Mol. Phys.*, 2015, **113**, 698-702.
39. S. Y. WU, J. S. YAO, H. M. ZHANG and G. D. LU, *Int. J. Mod. Phys. B*, 2007, **21**, 3250-3253.
40. K. Min-Quan, W. Shao-Yi, H. Xian-Fen and S. Bo-Tao, *Z. Naturforsch. A*, 2013, **68**, 442-446.
41. G. W. Burdick\* and M. F. Reid, *Mol. Phys.*, 2004, **102**, 1141-1147.

42. M. Karbowski, C. Rudowicz and P. Gnutek, *Opt. Mater.*, 2011, **33**, 1147-1161.
43. M. Karbowski, P. Gnutek and C. Rudowicz, *Chem. Phys.*, 2012, **400**, 29-38.
44. B. N. Figgis and M. A. Hitchman, 1999.
45. B. Henderson and R. H. Bartram, *Crystal-field engineering of solid-state laser materials*, Cambridge University Press, 2005.
46. M. Wildner, M. Andrut, C. Rudowicz, A. Beran and E. Libowitzky, *Spectroscopic methods in mineralogy*, 2004, **6**, 93-140.
47. C. Rudowicz and S. K. Misra, *Appl. Spectrosc. Rev.*, 2001, **36**, 11-63.
48. J. Mulak and Z. Gajek, *The effective crystal field potential*, Elsevier, 2000.
49. D. J. Newman and B. Ng, *Crystal field handbook*, Cambridge University Press, 2000.
50. C. Rudowicz, *J. Phys. C* 1985, **18**, 1415.
51. C. Rudowicz and C. Chung, *J. Phys. Condens. Matter.*, 2004, **16**, 5825.
52. F. Aquilante, J. Autschbach, R. K. Carlson, L. F. Chibotaru, M. G. Delcey, L. De Vico, I. Fdez. Galván, N. Ferré, L. M. Frutos, L. Gagliardi, M. Garavelli, A. Giussani, C. E. Hoyer, G. Li Manni, H. Lischka, D. Ma, P. Å. Malmqvist, T. Müller, A. Nenov, M. Olivucci, T. B. Pedersen, D. Peng, F. Plasser, B. Pritchard, M. Reiher, I. Rivalta, I. Schapiro, J. Segarra-Martí, M. Stenrup, D. G. Truhlar, L. Ungur, A. Valentini, S. Vancoillie, V. Veryazov, V. P. Vysotskiy, O. Weingart, F. Zapata and R. Lindh, *J. Comput. Chem.*, 2016, **37**, 506-541.
53. N. F. Chilton, R. P. Anderson, L. D. Turner, A. Soncini and K. S. Murray, *J. Comput. Chem.*, 2013, **34**, 1164-1175.
54. K. S. Cole and R. H. Cole, *J. Chem. Phys.*, 1941, **9**, 341-351.
55. J. A. Weil and J. R. Bolton, *Electron Paramagnetic Resonance, Elemental Theory and Practical Applications*, Wiley, New York, 2007.
56. B. J. Hathaway and D. E. Billing, *Coord. Chem. Rev.*, 1970, **5**, 143-207.
57. P. Sivaprasad, K. Ramesh and Y. P. Reddy, *Phys. Status Solidi B*, 1990, **118**, K103-K106.
58. D. E. Billing, R. J. Dudley, B. J. Hathaway and A. A. G. Tomlinson, *J. Chem. Soc. A*, 1971, DOI: 10.1039/J19710000691, 691-696.
59. E. Garribba and G. Micera, *J. Chem. Educ.*, 2006, **83**, 1229.
60. P. P. M. Valko, S. Biskupič, and M. Mazúr, *Chem. Pap.*, 1990, **44**, 805-813.
61. T. Pilati and A. Forni, *J. Appl. Crystallogr.*, 1998, **31**, 503-504.
62. T. Pilati and A. Forni, *J. Appl. Crystallogr.*, 2000, **33**, 417-417.
63. L. J. Farrugia, *J. Appl. Crystallogr.*, 2012, **45**, 849-854.
64. A. Wodyński and M. Kaupp, *J. Phys. Chem. A*, 2019, **123**, 5660-5672.
65. F. Neese, *J. Chem. Phys.*, 2003, **118**, 3939-3948.
66. K. J. de Almeida, Z. Rinkevicius, H. W. Hugosson, A. C. Ferreira and H. Ågren, *Chem. Phys.*, 2007, **332**, 176-187.
67. S. Hirata and M. Head-Gordon, *Chem. Phys. Lett.*, 1999, **314**, 291-299.
68. T. Shiozaki and T. Yanai, *J. Chem. Theory. Comput.*, 2016, **12**, 4347-4351.
69. C. Rudowicz and R. Bramley, *J. Chem. Phys.*, 1985, **83**, 5192-5197.
70. C. Rudowicz and P. Gnutek, *Physica B*, 2010, **405**, 113-132.
71. C. Rudowicz, in Ng, B. & Newman D.J., *Computer package CST: conversions, standardization and transformations*, Cambridge University Press Cambridge, 2000, pp 259.
72. C. Rudowicz and Q. Jian, *Comput. & Chem.*, 2002, **26**, 149-157.
73. C. Rudowicz, P. Gnutek and M. Karbowski, *Phys. Rev. B*, 2007, **76**, 125116.
74. H.-G. Liu, P. Gnutek and C. Rudowicz, *J. Lumin.*, 2011, **131**, 2690-2696.
75. C. Rudowicz, M. Karbowski, P. Gnutek and M. Lewandowska, *J. Phys. Condens. Matter.*, 2014, **26**, 065501.
76. C. Rudowicz, D. Yadav, R. Kripal and P. Gnutek, *J. Alloys Compd.*, 2016, **666**, 468-475.
77. R. Kripal, D. Yadav, P. Gnutek and C. Rudowicz, *J. Phys. Chem. Solids*, 2009, **70**, 827-833.
78. R. Peřka and C. Rudowicz, *Physica B*, 2016, **497**, 14-18.
79. C. Rudowicz and K. Tadyszak, *Polyhedron*, 2017, **127**, 126-134.
80. L. Chao-Ying, H. Ying and Z. Xue-Mei, *Physica B*, 2015, **456**, 125-128.
81. M.-Q. Kuang, S.-Y. Wu and H.-M. Zhang, *Optik*, 2012, **123**, 1601-1604.
82. M.-Q. Kuang, S.-Y. Wu, X.-F. Hu and B.-T. Song, *Physica B*, 2013, **417**, 13-16.

83. Y. Y. Yeung and C. Rudowicz, *Comput. & Chem.*, 1992, **16**, 207-216.
84. A. Drzewiecki, B. Padlyak, V. Adamiv, Y. Burak and I. Teslyuk, *Nukleonika*, 2013, **58**, 379--385.
85. R. Ravikumar, R. Komatsu, K. Ikeda, A. Chandrasekhar, B. Reddy, Y. Reddy and P. S. Rao, *J. Phys. Chem. Solids*, 2003, **64**, 261-264.
86. A. Mielcarek, A. Bieńko, P. Saramak, J. Jezierska and A. Dołęga, *Dalton Trans.*, 2019, **48**, 17780-17791.